


Aging-related tau astroglipathy (ARTAG): Not only tau phosphorylation in astrocytes

Isidro Ferrer MD, PhD^{1,2,3,4,CA}, Meritxell Aguiló García¹, Irene López González PhD³, Daniela Diaz Lucena PhD³, Aina Roig Villalonga¹, Margarita Carmona Tech^{1,3}, , Franc Llorens PhD³, Paula Garcia-Esparcia PhD², Alejandra Martinez-Maldonado¹, Margalida Frau Mendez¹, Benjamín Torrejón Escribano⁵, Joan Josep Bech Serra PhD⁶, Eduard Sabido, PhD⁷, Carolina de la Torre Gómez PhD⁶, José Antonio del Río PhD^{3,4,8}

¹Department of Pathology and Experimental Therapeutics, University of Barcelona;

²Senior Consultant, Bellvitge University Hospital, IDIBELL (Bellvitge Biomedical Research Centre); ³CIBERNED (Network Centre of Biomedical Research of Neurodegenerative Diseases), Institute of Health Carlos III, Ministry of Economy and Competitiveness; ⁴Institute of Neurosciences, University of Barcelona; ⁵Biology Unit, Scientific and Technical Services, University of Barcelona, Hospitalet de Llobregat;

⁶Proteomics platform, IDIBELL, Hospitalet de Llobregat; ⁷ Proteomics Unit, Centre de Regulació Genòmica, Barcelona Institute of Science and Technology, Barcelona;

⁸Molecular and Cellular Neurobiotechnology, Institute of Bioengineering of Catalonia (IBEC), Barcelona Institute for Science and Technology, Parc Científic de Barcelona, Barcelona; Spain

CA: Prof. I. Ferrer, Department of Pathology and Experimental Therapeutics, University of Barcelona, Feixa Llarga sn, 08907 Hospitalet de Llobregat, Spain; email: 8082ifa@gmail.com

Running title: ARTAG

Financial disclosure and conflict of interests

No relevant data.

Funding

This study was funded by Ministry of Economy and Competitiveness, Institute of Health Carlos III – Fondos FEDER, a way to build Europe: FIS PIE14/00034 and PI17/00809 to IF; and 13FIS037 and PT13/0001/0033 to IDIBELL Proteomics Unit, ProteoRed, PRB2-ISCIII; and Miguel Servet - CP16/00041 to FLI.

This article has been accepted for publication and undergone full peer review but has not been through the copyediting, typesetting, pagination and proofreading process which may lead to differences between this version and the Version of Record. Please cite this article as an 'Accepted Article', doi: 10.1111/bpa.12593

Abstract

Aging-related tau astrogliopathy (ARTAG) is defined by the presence of two types of tau-bearing astrocytes: thorn-shaped astrocytes (TSAs) and granular/fuzzy astrocytes in the brain of old-aged individuals. The present study is focused on TSAs in rare forms of ARTAG with no neuronal tau pathology or restricted to entorhinal and transentorhinal cortices, to avoid bias from associated tauopathies. TSAs show 4Rtau phosphorylation at several specific sites and abnormal tau conformation, but they lack ubiquitin and they are not immunostained with tau-C3 antibodies which recognize truncated tau at Asp421. Astrocytes in ARTAG have atrophic processes, reduced glial fibrillary acidic protein (GFAP), and increased superoxide dismutase 2 (SOD2) immunoreactivity. Gel electrophoresis and western blotting of sarkosyl-insoluble fractions reveal a pattern of phospho-tau in ARTAG characterized by two bands of 68kDa and 64kD, and several middle bands between 35kDa and 50kDa which differ from what is seen in AD. Phosphoproteomics of dissected vulnerable regions identifies an increase of phosphorylation marks in a large number of proteins in ARTAG compared with controls. GFAP, aquaporin 4, several serine-threonine kinases, microtubule associated proteins, and other neuronal proteins are among the differentially phosphorylated proteins in ARTAG thus suggesting a hyper-phosphorylation background that affects several molecules, including many kinases and proteins from several cell compartments and various cell types. Finally, present results show for the first time that tau seeding is produced in neurons of the hippocampal complex, astrocytes, oligodendroglia and along fibers of the corpus callosum, fimbria, and fornix following inoculation into the hippocampus of wild type mice of sarkosyl-insoluble fractions enriched in hyper-phosphorylated tau from selected ARTAG cases. These findings show astrocytes as crucial players of tau seeding in tauopathies.

Key words: ARTAG, thorn-shaped astrocytes, kinases, tau, seeding, phosphorylation

Introduction

Aging-related tau astrogliopathy (ARTAG) is defined by the presence of two types of tau-bearing astrocytes: thorn-shaped astrocytes (TSAs) and granular/fuzzy astrocytes (GFAs) in the brain of old-aged individuals (28). TSAs are a variety of fibrillar astrocyte characterized by a thorn-like appearance, located in the subependymal and subpial regions, perivascular spaces, and in clusters in the frontal and temporal cortices, basal forebrain, and brain stem (16, 21, 22, 23, 30, 36, 37, 40, 49, 54). TSAs were first described in association with Alzheimer's disease (AD) and argyrophilic grain disease (AGD) but they are also common in other tauopathies in the elderly (29, 31). GFAs are mainly located in the grey matter; firstly identified in a particular subgroup of patients with dementia in the elderly (30), they are also present in combination with other tauopathies in the elderly (14).

TSAs in advanced stages of AD show tau phosphorylation at several specific sites and abnormal tau conformation, but they lack ubiquitin and are not immunostained with tau-C3 antibodies which recognize truncated tau at Asp421 (37). Gel electrophoresis and western blotting to phospho-tau of sarkosyl-insoluble fractions from TSAs-containing white matter showed a pattern of two bands of 68kDa and 64 kDa typical of 4R-tauopathies in contrast with the phospho-tau band pattern of AD characterized by three bands of 68kDa, 64kDa, and 60kDa, and a lower band of truncated tau of about 20 kDa obtained from the neurofibrillary tangle (NFT)-rich dissected hippocampus of the same cases (37). Therefore, TSAs in AD are 4Rtau astrocytes with immunohistochemical properties of pre-tangles (14).

Pioneering studies have demonstrated seeding and spreading of abnormal tau derived from brain homogenates of AD and other tauopathies inoculated into the brain of transgenic mice over-expressing human tau or mutated tau under the rationale that this background facilitates tau seeding and propagation (4, 7, 34). The characteristics of seeding differ depending on the type of tauopathy, thus suggesting that several types of tau species have particular properties (8, 41). Recent studies have shown seeding of human tau from homogenates of AD and tauopathy cases inoculated into the brain of wild-type mice, thereby indicating that a potentiating background is not mandatory to trigger this process (19, 41). All these experiments were performed using brain samples with tau pathology only in neurons, or in neurons and glial cells. None of these studies enabled the examination of glial tau as the source of abnormal tau seeding. This is an important aspect because neurodegenerative diseases are not restricted to neurons but rather involve neurons and glial cells (12, 44, 45, 58).

The present study is designed to delve further into the characteristics of tau deposition, and the properties and environment of TSAs in ARTAG cases with maximal tau deposition limited to the entorhinal and transentorhinal cortex (Braak and Braak stages I-II of NFT pathology) to avoid bias linked to associated tauopathies. The study is focused on four main aspects: i. biochemical characteristics of tau, ii. properties of TSAs, iii. assessment of the phosphoproteome and identification of phosphorylated proteins in TSA-enriched temporal white matter to characterize the biochemical environment in which TSAs develop, and iv. capacity of tau seeding of sarkosyl-insoluble fractions from ARTAG cases inoculated into the hippocampus of wild-type mice, and identification of cell targets of tau seeding.

Material and methods

Brain samples

Brain tissue was obtained from the Institute of Neuropathology HUB-ICO-IDIBELL Biobank following the guidelines of Spanish legislation on this matter (Real Decreto de Biobancos 1716/2011) and approval of the local ethics committee. One hemisphere was immediately cut in coronal sections, 1cm thick, and selected areas of the encephalon were rapidly dissected, frozen on metal plates over dry ice, placed in individual air-tight plastic bags, and stored at -80°C until use for biochemical studies. The other hemisphere was fixed by immersion in 4% buffered formalin for 3 weeks for morphological studies; sections from twenty representative brain regions were stained with hematoxylin and eosin, periodic acid-Schiff (PAS) and Klüver-Barrera, or processed for immunohistochemistry for microglia Iba1, GFAP, β -amyloid, A β 40, A β 42, phospho-tau AT8, α -synuclein, TDP-43, ubiquitin, p62C and p62N, using EnVision+ System peroxidase (Dako), and diaminobenzidine and H₂O₂. Details of the antibodies are shown in Table I.

NFT stages were categorized according to Braak and Braak modified for paraffin sections (5, 6). Since the present series of ARTAG was restricted to cases with no neuronal pathology or with NFTs and pre-tangles limited to the entorhinal and entorhinal cortex without β -amyloid deposition, the possibility that some cases had associated primary age-related tauopathy (PART) (9) cannot be excluded. Staging of argyrophilic grain disease (AGD) was established as reported elsewhere (16). Chronic traumatic encephalopathy (35) was not recorded in any case.

Control cases had not suffered from neurologic or psychiatric diseases, infections of the nervous system, brain neoplasms, or systemic and central immune diseases, and did not have abnormalities in the neuropathological examination. Cases with associated pathologies such as vascular diseases (excepting mild atherosclerosis and arteriolosclerosis), TDP-43 proteinopathy, metabolic syndrome, and hypoxia were excluded from the present study.

ARTAG cases were six men and two women aged 77 ± 8.6 years. ARTAG lesions were categorized as detailed elsewhere (31). Semi-quantitative assessment of optical microscopy sections was performed separately by at least two people. The abundance of THAs, as revealed in AT8-immunostained sections, was categorized as: ++ for large and + for small numbers of positive cells/inclusions, and – for no immunoreactivity. The characteristics of cases and the distribution of lesions in each case are summarized in Table II.

Control cases were four men and four women aged 66.3 ± 5.5 years. In addition, the frontal cortex of two AD cases stages V-VI/C (one man aged 74 and one woman aged

78) was used in the study of phospho-tau band patterns from sarkosyl-insoluble fractions. The cause of death in ARTAG and control cases was variable and included bronchopneumonia, respiratory failure, cardiac arrest, kidney failure, pulmonary thromboembolism, and metastatic carcinoma. Post-mortem delay between death and tissue processing was between 4h and 18h in ARTAG and control cases.

All cases were used for immunohistochemistry, immunofluorescence and confocal microscopy, and RT-qPCR. Cases 3 (medulla oblongata, basal forebrain), 5, and 7 (basal forebrain and caudate) were used for the extraction of sarkosyl-insoluble fractions and western blotting studies of tau. Cases 2 (medulla oblongata), 3, and 6 (temporal white matter) were used for phosphoproteomics.

Sarkosyl-insoluble fractions used for inoculation were obtained from the medulla oblongata and basal forebrain of an 87-year-old woman with PART1 (case 3); and from the basal forebrain and caudate of two men aged 75 and 70 years with neuropathological diagnoses of PART2 and Lewy body disease stage 3, respectively (cases 5 and 7) (Table II).

Importantly, all the samples used for inoculation studies were first checked for morphological changes in cryostat sections stained with anti-tau antibodies. Although the preservation of the material was suboptimal due to freezing, it was suitable to verify the presence of large numbers of TSAs and the lack of tau pathology in other cell types including neurons (as expected from the screening and selection of cases in the present series) and oligodendrocytes.

Control and ARTAG cases were processed in parallel in all assessments.

Immunohistochemistry

De-waxed sections, 4 microns thick, were processed for immunohistochemistry. The sections were boiled in citrate buffer (20min) to retrieve tau antigenicity. Endogenous peroxidases were blocked by incubation in 10% methanol-1% H₂O₂ solution (15min) followed by 3% normal horse serum solution. Then the sections were incubated at 4°C overnight with one of the primary antibodies against 4Rtau, 3Rtau, amino acids 14-26 (antibody 499), amino acids 229-233 (antibody 229), amino acids 394-398), specific phospho-tau Thr181, Ser199, Thr231, Ser262 and Ser422, double-phosphorylation sites Ser202-Thr205 (clone AT8), Ser396-404 (PHF1) and Thr212-Ser214 (tau-100), conformational tau modifications at amino acids 5-15 (Alz50) and amino acids 312-322 (MC-1), and tau truncated at aspartic acid 421 (tau-C3). Other sections were incubated with one of the following antibodies against glial fibrillary acidic protein (GFAP): P-GFAP Ser8, phosphorylated tuberin (P-tuberin Ser939), superoxide dismutase 2 (SOD2), aquaporin 4 (AQP4), phosphorylated p38 (p38-P Thr180-Tyr182), phosphorylated protein kinase A α/β (PKA-P α/β Thr197), glutamate transporter solute

carrier family 1, member 2 (GLT-1/EAAT2), vimentin and YKL-40. The characteristics of the antibodies, dilutions, and suppliers are listed in Table I.

Following incubation with the primary antibody, the sections were incubated with EnVision + system peroxidase (Dako, DK) for 30 min at room temperature. The peroxidase reaction was visualized with diaminobenzidine and H₂O₂. Control of the immunostaining included omission of the primary antibody; no signal was obtained following incubation with only the secondary antibody.

Double-labeling immunofluorescence and confocal microscopy in human cases

De-waxed sections, 4 microns thick, were stained with a saturated solution of Sudan black B (Merck, DE) for 15 min to block autofluorescence of lipofuscin granules present in cell bodies, and then rinsed in 70% ethanol and washed in distilled water. The sections were boiled in citrate buffer to enhance antigenicity and blocked for 30 min at room temperature with 10% fetal bovine serum diluted in PBS. Then, the sections were incubated at 4°C overnight with combinations of primary antibodies against phospho-tau Thr181, and antibodies 499 and 394; P-GFAP Ser8 and phospho-tau Thr181; and AT8 and SOD2, vimentin, YKL-40, P-tuberin, GLT-1, AQP4, p38-P Thr180-Tyr182, and P-PKA α/β Thr197.

The characteristics of the antibodies, dilutions, and suppliers are listed in Table I.

After washing, the sections were incubated with Alexa488 or Alexa546 (1:400, Molecular Probes, USA) fluorescence secondary antibodies against the corresponding host species. Nuclei were stained with DRAQ5TM (1:2,000, Biostatus, GB). After washing, the sections were mounted in Immuno-Fluore mounting medium (ICN Biomedicals, USA), sealed, and dried overnight. Sections were examined with a Leica TCS-SL confocal microscope.

Image acquiring and analysis

Confocal images were acquired using a microscope Leica DMIRE2 and Leica confocal software. Quantification of GFAP positive cell area and size was performed using Fiji ImageJ software in three different sections containing between 25-100 cells per image.

Statistical Analysis

Statistical analysis was performed using GraphPad Prismv5 software. Differences between groups were analyzed by one-way ANOVA followed by the appropriate post-hoc test.

Normalization of antibody-based protein detection

Series of cases were processed in parallel to equalize the conditions of staining of a particular antibody in sections from different entities, and a given antibody was used in different series to minimize day-to-day variations. The estimation of co-localization of two proteins labeled with specific antibodies and examined with the confocal

microscope was assessed by counting the number of cells expressing both antigens in relation to the number of cells stained with each one of the antibodies in five selected fields per section at a magnification of x600 in every case. In most instances, the values were expressed as the percentage of the more abundant protein because the less abundant protein represented a subset of the former.

Western blotting of sarkosyl-insoluble fractions

Frozen samples of about 1g were lysed in 10 volumes (w/v) with cold suspension buffer (10mM Tris-HCl, pH 7.4, 0.8M NaCl, 1mM EGTA) supplemented with 10% sucrose, protease, and phosphatase inhibitors (Roche, GE). The homogenates were first centrifuged at 20,000×g for 20min (Ultracentrifuge Beckman with 70Ti rotor) and the supernatant (S1) was saved. The pellet was re-homogenized in 5 volumes of homogenization buffer and re-centrifuged at 20,000×g for 20min (Ultracentrifuge Beckman with 70Ti rotor). The two supernatants (S1 + S2) were then mixed and incubated with 0.1% N-lauroylsarkosylate (sarkosyl) for 1h at room temperature while being shaken. Samples were then centrifuged at 100,000×g for 1h (Ultracentrifuge Beckman with 70Ti rotor). Sarkosyl-insoluble pellets (P3) were re-suspended (0.2 ml/g) in 50mM Tris-HCl (pH 7.4). Protein concentrations were quantified with the bicinchoninic acid assay (BCA) assay (Pierce, Waltham, MA). Samples were mixed with loading sample buffer and heated at 95°C for 5min. 60ug of protein was separated by electrophoresis in SDS-PAGE gels and transferred to nitrocellulose membranes (200mA per membrane, 90 min). The membranes were blocked for 1h at room temperature with 5% non-fat milk in TBS containing 0.2% Tween and were then incubated with one of the primary antibodies: anti-tau Ser422 (diluted 1:1000; Thermo Fisher (Waltham, MA, USA), or anti-4Rtau (diluted 1:1,000; Millipore). After washing with TBS-T, blots were incubated with the appropriate secondary antibody (anti-mouse/anti-rabbit IgG conjugated with horseradish peroxidase diluted at 1:2,000, DAKO, DE) for 45min at room temperature. Immune complexes were revealed by incubating the membranes with chemiluminescence reagent (Amersham, GE Healthcare, Buckinghamshire, UK).

Phosphoproteomics

Sample preparation, phosphopeptide enrichment, and LC-MSMS analysis

Three control and three ARTAG fresh brain samples were processed for protein extraction in 7M urea, 2M thiourea, and 2% SDS. After that, samples were quantified using the BCA method and 350µg of every sample condition was digested using a FASP (Filter-Aided Sample Preparation) approach. Briefly, proteins were reduced with dithiothreitol 10mM (60min, 32°C) and alkylated with iodoacetamide 20mM (30min at 25°C in the dark). Then, the samples were loaded onto an Amicon Ultra (filter 10KDa,

0.5mL, Millipore, Billerica, MA, USA) device to remove interfering agents with 2 rounds of centrifugations/washes with 100mM ammonium bicarbonate buffer (13,600g; 25min at room temperature). Digestion was carried out in two steps: first, samples were digested (1:50w sample/w enzyme) with Lys-C (Wako, Richmond, VA, USA) in 6M urea buffer for 3h at 35°C, second, the samples were diluted 10-fold with 100mM ammonium bicarbonate buffer and digested with modified porcine trypsin (Promega-Gold, Madison, WI, USA) (1/25w sample/w enzyme) for 16h at 37°C. The resulting peptide mixture was recovered by centrifuging the filter. Then, the filter was washed twice with 300µL of 50mM ammonium bicarbonate and once with 200µL of 20% acetonitrile/50mM ammonium bicarbonate (13,600g for 25min at room temperature). All the fractions were pooled, and the final peptide mixture was acidified with formic acid. Finally, the final volume of the acidified peptide solution was reduced on a SpeedVac vacuum system (Thermo Fisher Scientific, Barcelona, Spain), and the peptide solution was desalinated with a C₁₈ spin column (Thermo Fisher Scientific) following the indications of the supplier. An aliquot of 200µg was separated and further processed for phosphopeptide enrichment.

Phosphopeptide enrichment was carried out with titanium dioxide (TiO₂) magnetic beads following the specifications of the supplier (High-Select™ TiO₂ Phosphopeptide Enrichment Kit, Thermo Fisher Scientific). Briefly, peptides were re-suspended by vortexing in 150µL of binding/equilibration buffer at pH <3. Then, the phosphopeptides were enriched with the TiO₂ beads and finally dried in a SpeedVac under vacuum.

Samples were analyzed in a Proxeon 1000 liquid chromatographer coupled to an Orbitrap Fusion Lumos (Thermo Fisher Scientific) mass spectrometer. Samples were re-suspended in 0.5% formic acid in water, and 4.5µL were injected for LC-MS/MS analysis. Peptides were trapped on an NTCC-360/75-3-123 LC column and separated using a C₁₈ reverse phase LC column-Easy Spray (Thermo Fisher Scientific). The gradient used for the elution of the peptides was 1% to 35% in 90min followed by a gradient from 35% to 85% in 10min with 250nL/min flow rate. Eluted peptides were subjected to electrospray ionization in an emitter needle (PicoTip™, New Objective, Scientific Instrument Services, Ringoes, NJ, USA) with an applied voltage of 2,000V. Peptide masses (*m/z* 300-1700) were analyzed in data-dependent mode where a full scan MS was acquired on the Orbitrap with a resolution of 60,000 FWHM at 400m/z. Up to the 10 most abundant peptides (minimum intensity of 500 counts) were selected from each MS scan and then fragmented using CID (collision-induced dissociation) in the linear ion trap using helium as collision gas with 38% normalized collision energy. Multistage activation was enabled to favor the detection of phosphopeptides. The scan

time settings were: full MS at 250ms and MSn at 120ms. Generated .raw data files were collected with Thermo Xcalibur (v.2.2) (Termo Fisher Scientific).

Database search

Thermo Proteome Discoverer (v. 2.0.0.802) was used to search the .raw data obtained in the MS analyses against a SwissProt/Uniprot human database with the MASCOT search engine (v2.5). A target and decoy database was used in combination with the Percolator algorithm to assess the false discovery rate (FDR). The PhosphoRS node was used to provide a confidence measure for the localization of phosphorylation in the peptide sequences identified with this modification.

Phosphopeptides analysis

Before proceeding to the statistical analysis data were pre-processed in four sequential steps. (i) the phosphopeptide list was filtered in order to remove potential contaminants (i.e., residual peptides bound to the chromatographic column such as bovine serum proteins); (ii) phosphopeptides with the identical amino acid sequence as well as phosphosites were merged into a single phosphopeptide (i.e., methionine-oxidized and non-methionine oxidized phosphopeptides); (iii) the information on the multi-phosphorylated peptides was split so that each phosphosite appears in a single row; and (iv) the final list of phosphosites was filtered to retain only the sites with a probability site value (pRS) greater than 75% (0.75). After that, missing not at random areas (MNAR) were imputed using the minimal area value detected in every run by the mass spectrometer. Missing values were considered MNAR when three valid values appear in one experimental condition and only one or no valid values appear in the other condition.

Before the imputation step, the quantification values for every sample were log2-normalized against the corresponding median. In order to avoid potential bias introduced by the phosphopeptide enrichment, this value is calculated, for every sample, using the intensity values of the total peptides. Finally, a two-sided t-test was performed for every phosphosite and the p-value adjusted by False Discovery Rate using the Benjamini-Hochberg procedure.

Phosphomotif enrichment analysis

The enrichment of potential phosphorylation motifs was performed using the motif-X web tool (<http://motif-x.med.harvard.edu/>) (50). Previous to the analysis, the phosphosites of interest were centered, using the canonical sequence for every protein in the human uniprot database, so that a final 15-mer was obtained for every phosphosite. The list of 15-mers was analysed at motif-x. The searching parameters used were “centered”, “foreground format,” and “width” or number of total characters in the motif (in our samples, “width”=15). The rest of the parameters were set by default.

RNA purification, retrotranscription reaction and RT-qPCR for detection of 3R and 4R tau isoforms

Purification of RNA from the temporal white matter in control, AD and ARTAG cases was carried out using RNeasy Lipid Tissue Mini Kit (Qiagen, Hilden, Germany) following the protocol provided by the manufacturer combined with DNase digestion to avoid extraction and later amplification of genomic DNA. The concentration of each sample was obtained from A260 measurements with NanoDrop 2000 spectrophotometer (Thermo Scientific, Waltham, MA, USA). RNA integrity was tested using the Agilent 2100 BioAnalyzer (Agilent, Santa Clara, CA, USA). Retrotranscription reaction of RNA samples was carried out with the High-Capacity cDNA Archive kit (Applied Biosystems, Foster City, CA, USA) following the guidelines provided by the supplier, and using Gene Amp® 9700 PCR System thermocycler (Applied Biosystems). A parallel reaction for one RNA sample was processed in the absence of reverse transcriptase to rule out DNA contamination. Tau mRNA isoforms were assessed by using SYBR green quantitative RT-PCR; 1,000ng of total RNA was used as a template. cDNA samples obtained from the retrotranscription reaction were diluted 1:20 and duplicate SYBR green PCR assays for each gene were performed. For each reaction, 2.5µl of cDNA was mixed with 1.25µl of forward primer 10µM, 1.25µl reverse primer 10µM and 5µl of PowerUp™ SYBR® Green Master Mix (Applied Biosystems). The reactions were performed following the parameters: 50°C for 2 min, 95°C for 10 min, and 40 cycles at 95°C for 15 sec and at 60°C for 1 min. SYBR green PCR data were captured using the Sequence Detection Software (SDS version 2.2, Applied Biosystems). Forward and reverse primer sequences for quantitative PCR were 3Rtau forward: GTCCGTA CTCCACCCAAGTC; 3Rtau reverse: GTTTGTAGACTATTTGCACCTTC; 4Rtau forward: GGCGGGAAGATGCAGATAATTAAT; 4Rtau reverse: GTAGACTATTTGCACACTGCC. Parallel assays for each sample were carried out using primers for β-glucuronidase (*GUS-β*) forward: GTCTGCGGCATTTTGTCCG, reverse: CACACGATGGCATAGGAATGG; X-prolyl aminopeptidase P1 (*XPNPEP1*) forward: CTCATTCCTGTCAAGGAGAACC, reverse: ACCACATGACGTTCTCTCAG; and glyceraldehyde-3-phosphate dehydrogenase (*GADPH*) forward: CGCTCTCTGCTCCTCTGTT and reverse: CCATGGTGTCTGAGCGATGT; as endogenous controls. For the data analysis, threshold cycle (CT) values for each sample were processed to obtain the double delta CT ($\Delta\Delta CT$) values. First, delta CT (ΔCT) values were calculated as the normalized CT values of each target gene in relation to the CT of endogenous controls *GUS-β*, *XPNPEP1* and *GADPH*. Then, $\Delta\Delta CT$ values were obtained from the ΔCT of each sample minus the mean ΔCT of the

population of control samples. The fold change was calculated using the equation $2^{(-\Delta\Delta CT)}$. Mean fold-change values of each experimental group were analyzed by One Way ANOVA test with post-hoc Tukey by using GraphPad Prism version 5.01 (La Jolla, CA, USA) and Statgraphics Statistical Analysis and Data Visualization Software version.1 (Warrenton, VA, USA).

Animals and tissue processing

All animal procedures were carried out following the guidelines of the European Communities Council Directive 2010/63/EU and with the approval of the local ethical committee (University of Barcelona, Spain).

Wild-type C57BL/6 mice were injected into the hippocampus at the coordinates AP: -1.9, ML: ± 1.4 and DV: -1.5 for 10 min, followed by a waiting time of 5 min and removal of the needle 10 min later; or into the lateral ventricle at the coordinates AP: -0.6, ML: ± 1.2 and DV: -2.2 for 15 min, followed by a waiting time of 4 min and removal of the needle 15 min later. The quantity injected was 0.8 μ L in every case. Each mouse was injected with inoculum from a single ARTAG (or AD) case. Animals were killed under anaesthesia at the desired time-periods and the brains were rapidly fixed with paraformaldehyde in phosphate buffer and embedded in paraffin. Consecutive serial sections 4 μ m thick were obtained with a sliding microtome; sections were stained with haematoxylin and eosin or processed for immunohistochemistry using the antibody AT8), 4Rtau and 3Rtau. Following incubation with the primary antibody, the sections were incubated with EnVision + system peroxidase for 30 min at room temperature. The peroxidase reaction was visualized with diaminobenzidine and H₂O₂. Control of the immunostaining included omission of the primary antibody; no signal was obtained following incubation with only the secondary antibody.

Double-labeling immunofluorescence was carried out on de-waxed sections, 4 μ m thick, which were stained with a saturated solution of Sudan black B (Merck, DE) for 15 min to block autofluorescence of lipofuscin granules present in cell bodies, and then rinsed in 70% ethanol and washed in distilled water. The sections were boiled in citrate buffer to enhance antigenicity and blocked for 30 min at room temperature with 10% foetal bovine serum diluted in PBS. Then, the sections were incubated at 4°C overnight with combinations of AT8 and one of the following primary antibodies: GFAP, Iba-1, Olig2 and p38-P Thr180-Tyr182. Other sections were immunostained with anti-phospho tauThr181 and anti-NeuN (see Table I for the characteristics of the antibodies). After washing, the sections were incubated with Alexa488 or Alexa546 fluorescence secondary antibodies against the corresponding host species. Nuclei were stained with DRAQ5™. After washing, the sections were mounted in Immuno-Fluore mounting

medium, sealed, and dried overnight. Sections were examined with a Leica TCS-SL confocal microscope.

Results

TSAs were recognized using AT8 antibodies and 4Rtau immunoreactivity, but they were negative with anti-3Rtau antibodies. TSAs were localized in subpial and subependymal regions, perivascular areas, clusters in the temporal and frontal white matter, basal forebrain, caudate, amygdala (including white matter surrounding the amygdala), and medulla oblongata. The distribution of TSAs was subject to individual variations; its characteristics in every case are summarized in Table II.

In agreement with our previous characterization of TSAs in AD (37), THAs in the present series were stained with specific tau antibodies against phospho-Thr181, phospho-Ser199, phospho-Thr231, phospho-Ser262, and phospho-Ser422, double-phosphorylation sites phospho-Ser202-phospho-Thr205 (clone AT8) and phospho-Ser396-404 (PHF1), conformational tau modifications at amino acids 5-15 (Alz50), and amino acids 312-322 (MC-1). TSAs were negative with antibodies against tau truncated at aspartic acid 421 (tau-C3). In addition, TSAs were stained with antibodies 499 (recognizing amino acids 14-26), 229 (amino acids 229-233), and 394 (amino acids 394-398), and with antibody anti-tau-100 (phospho-Thr212/Ser214) (Figure 1 A-L). Double-labeling immunofluorescence and confocal microscopy with antibody 499 and specific tau antibody against phospho-Thr181, and with antibody 394 and anti-tau phospho-Thr181, disclosed 499 and 394 immunoreactivity in all TSAs (Figure 1 M, N).

TSAs, as revealed with GFAP immunohistochemistry, showed small size and reduced numbers of branches in frontal white matter, temporal white matter, subpial region, and subependymal region (Figure 2). This was in contrast not only with astrocytes in control, younger individuals but especially with neighbouring reactive GFAP-immunoreactive astrocytes in the same cases. Double-labeling immunofluorescence and confocal microscopy confirmed reduced GFAP immunoreactivity in TSAs (Figure 3).

YKL-40, used as a marker of inflammatory astrocytes (38), and vimentin was expressed in a subpopulation of astrocytes in control and ARTAG cases. The number of vimentin and YKL-40 positive astrocytes was higher in ARTAG when compared with controls in agreement with reactive astrogliosis (12). However, double-labelling immunofluorescence and confocal microscopy revealed reduced size and decreased number of immunoreactive processes in TSAs (Figure 4)

Band pattern of tau in sarkosyl-insoluble fractions

Dissected basal forebrain and medulla oblongata from ARTAG cases with abundant TSAs were processed in parallel with samples of the frontal cortex from AD cases stage V. Three phospho-tau bands (anti-tau phospho-Ser422) of 68kDa, 64kDa, and 60kDa were seen in the frontal cortex of cases with AD. In addition, several bands of

molecular weight between 50kDa and 30kDa together with a lower band of about 23kDa, of variable intensity among cases, were found in AD. These corresponded to two bands of 4R tau between 68 and 60kDa, and several bands of lower molecular weight stained visualized with specific anti-4R antibodies, respectively. In contrast, the band pattern of ARTAG phospho-tau using the same antibody and processed in parallel with AD samples showed two bands of 68kDa and 64kDa, and several bands of lower molecular weight corresponding to truncated forms of tau. The lower phospho-tau band of about 23kDa was absent in ARTAG cases. Curiously, one sample of the medulla oblongata showed a very weak band of 68kDa and a weak double-band at 64 kDa. Parallel membranes blotted with 4Rtau antibodies showed a doublet of 64kDa (Figure 5).

3Rtau and 4Rtau ratios

Although not significant, 3Rtau and 4Rtau mRNA expression levels were reduced in AD and ARTAG cases when compared with controls. The ratio 3Rtau/4Rtau was also reduced in AD and ARTAG cases when compared with controls. Yet no differences were seen between AD and ARTAG (Supplementary Figure 1)

SOD2, AQP4 and GLT-1 immunoreactivity

Single immunohistochemistry showed increased SOD2 immunoreactivity in subpial, subependymal, and some perivascular astrocytes, and in astrocytes of the white matter and basal forebrain in all cases with ARTAG when compared with middle-aged individuals. These findings were consistent with senescent modifications of astrocytes (18). Double-labeling immunofluorescence to SOD2 and phospho-tau clone AT8 revealed that TSAs and non-TSAs in the same tissue section were immunoreactive to SOD2 (Figure 6A).

AQP4 immunoreactivity was variable from one case to another, but in general terms it was more pronounced in the molecular layer, subependymal region, and basal forebrain in ARTAG in comparison with control samples. Individual variations did not permit a realistic quantitative validation in the present series. However, double-labeling immunofluorescence to AQP4 and tau AT8 in samples of the temporal white matter revealed AQP4 immunoreactivity at the cell membrane of TSAs. A similar pattern was seen in other glial cells in the temporal white matter with no phospho-tau deposition (Figure 6B).

GLT-1 immunoreactivity was present in astrocytes of the basal forebrain, temporal white matter, subpial region at the level of the medulla oblongata, and subependymal regions (the regions here assessed) in control and ARTAG cases. Double-labeling immunofluorescence and confocal microscopy to GLT-1 and hyper-phosphorylated tau

(clone AT8) identified GLT-1 immunoreactivity at the cell membrane of TSAs and non-TSAs in the same tissue section in ARTAG (Figure 6C).

Phosphoproteomics

Phosphosites differences between control and ARTAG cases, as seen in the heat map in Figure 7A, were imputed as MNAR. One-hundred twenty-two phosphosites showed higher abundance in ARTAG when compared to controls, and thirty-six phosphosites were more abundant in controls when compared to ARTAG (Supplementary Table 1). Since some proteins showed various sites of phosphorylation the total number of differentially phosphorylated proteins was 109 and 31, respectively, for ARTAG and controls (Table III). Several phosphorylated proteins with identification of phosphorylation positions are shown in Table IV. Among them, GFAP was found to be phosphorylated at positions 8, 14, 82, and 424, and aquaporin 4 was phosphorylated at position 273. Interestingly, many neuronal and glial proteins were differentially phosphorylated in ARTAG. These include proteins of the cytoskeleton, kinases, proteins linked to calcium/calmodulin signalling, cAMP signalling and DNA repair, nuclear and nucleolar regulators, proteins linked to tight junctions, proteins linked to proteolysis, and synaptic proteins, among others (Table III). A smaller number of proteins showed decreased levels of phosphorylated peptides in ARTAG when compared with controls (Table III). Regarding microtubule associated proteins (MAPs), phosphorylation of MAP-tau (as expected), MAP1A, MAP1AA, MAPK1S and MAP2 was greater in ARTAG, whereas phosphorylation of MAP1B, MAP4 and MAP6 was higher in controls.

Phosphomotif-enriched analysis revealed a motif enriched in ARTAG (SP). This motif is a phosphorylation site used for a wide number of kinases such as MAPK (including p38) and CDKs (Figure 7B).

Immunohistochemistry of selected phosphorylated proteins in ARTAG

Double-labeling immunofluorescence revealed that TSAs co-localized GFAP-P, PKA-P, and p38-P. GFAP-P was expressed in hyper-phosphorylated tau-bearing and non-hyper-phosphorylated tau-bearing astrocytes in the temporal white matter. TSAs co-localized active forms (phosphorylated at specific sites) of kinases p38 and PKA α/β . Tuberin-P was expressed in neurons of the hippocampus but not in tau-containing astrocytes (Figure 8).

Tau seeding in inoculated mice

Mice injected with AD fractions showed phospho-tau deposits in the fimbria, corpus callosum, and neurons of the hippocampus seven months after inoculation. The distribution and profile in the two mice inoculated with homogenates from two different AD cases was the same as the pattern already described by others (18) thus validating

those observations and serving as positive controls in the present series (data not shown).

The first group of six ARTAG-treated mice were injected at the age of seven months, three in the ventricle and three in the hippocampus, and killed at the age of ten months. No tau deposits were seen following intraventricular injection. However, intracellular deposits of hyper-phosphorylated tau were found in threads and in a few cells in the fimbria, lateral corpus callosum, and lateral part of the hippocampus in two of the three mice injected in the hippocampus (Figure 9A and B).

A second group of mice was injected into the hippocampus at the age of three months and killed at the age of ten months; four animals were inoculated with ARTAG and two with vehicle alone. All ARTAG-injected animals showed hyper-phosphorylated tau deposits in the fimbria, fornix, corpus callosum traversing the contralateral hemisphere, and the hippocampal complex including gyrus dentatus, CA1 and CA3 region of the hippocampus, and subiculum (Figure 9C-I). Curiously, cells were positive to 4Rtau (Figure 9J), as expected, but also to 3Rtau (Figure 9K and L). Double-labeling immunofluorescence and confocal microscopy disclosed hyper-phosphorylated tau deposition in neurons and astrocytes, as revealed with anti-NeuN and anti-GFAP antibodies, respectively, in animals with short interval between inoculation and examination (Figure 10A and B); microglia, as revealed with Iba-1 antibodies, did not contain hyper-phosphorylated tau (Figure 10C). Similar intracellular localization of hyper-phosphorylated tau was found in neurons and astrocytes in animals with long interval between inoculation and neuropathological examination, as revealed with the same antibodies; microglia did not contain hyper-phosphorylated tau deposits (Figure 11A, C, D, E and F). In addition, hyper-phosphorylated tau was found in oligodendroglia mainly in corpus callosum as revealed by double-labeling immunofluorescence using anti-Olig2 antibodies (Figure 11G and H). Finally, the possibility that hyper-phosphorylated tau deposition was an active process within seeds was sustained by co-localization of active p38 kinase (phosphorylated at Thr180-Tyr182) only in cells containing hyper-phosphorylated tau (Figure 11B).

Discussion

The morphological characteristics and distribution of TSAs in this ARTAG series with no tau deposition in neurons or with NFTs and pre-tangles restricted to the entorhinal and transentorhinal cortex are similar to those described in ARTAG associated with tauopathies (28, 29, 31, 36). The pattern of tau phosphorylation of TSAs identified here does not differ from TSAs associated with other tauopathies including AD and AGD (14, 37). Additional features of THAs include lack of evidence of truncated tau using specific antibodies against C-terminal and N-terminal regions, together with negativity to tau-C3 which recognizes truncated tau at Asp421. Gel electrophoresis and western blotting of sarkosyl-insoluble fractions show two bands of 68 kDa and 64 kDa (in some areas as a doublet) and several weaker bands of lower molecular weight. In no case are triple bands of 68kDa, 64kDa, and 60kDa and a lower band of truncated tau of about 20kDa, typical of AD, found in ARTAG. In conclusion, TSAs are composed of hyper-phosphorylated 4Rtau with features of pre-tangles lacking tau truncation at terminal regions.

Considering that TSAs are present in aged brains, further analysis was carried out to learn about categorization of these astrocytes and functional implications of this particular astrocytopathy (12). TSAs show reduced GFAP expression, reduced volume, and reduced numbers of branches. This was further recognized using anti-vimentin and YKL-40 antibodies. SOD2 immunoreactivity, which is augmented in senescent astrocytes (48), is increased in TSAs when compared with astrocytes of younger individuals. Yet these features are not restricted to TSAs but also apply to neighboring astrocytes with no hyper-phosphorylated tau deposition. Moreover, neighboring astrocytes show increased area coverage, and increased GFAP, vimentin and YKL-40 immunoreactivity. Therefore, TSAs are a subpopulation of astrocytes showing senescent features (18, 46, 48).

Astrocytes have specific functions mediated by selective molecules and pathways, among them the modulation of glutamate transport through astroglial glutamate transporter solute carrier family 1, member 2 (GLT-1/ EAAT2) (39, 42). Double-labeling immunofluorescence and confocal microscopy identifies GLT-1 immunoreactivity at the cell membrane of TSAs and non-TSAs in the same tissue sections. Decreased GLT-1 immunoreactivity in tau-containing astrocytes has been reported in a familial behavioral variant of frontotemporal dementia associated with astrocyte-predominant tauopathy, in which astrocytes show advanced stage of tangle formation with tau truncation and ubiquitination (13). GLT-1 expression is also altered in transgenic mice with astroglial tau phosphorylation (10); tau in transgenic mice is abnormally phosphorylated,

ubiquitinated, and filamentous; abnormal astrocytes are variably positive with thioflavine S (17). Therefore, relative preservation of GLT-1 in TSAs compared with astrocytes in the previous conditions may be related to the less advanced stage of cellular damage linked to tau phosphorylation and truncation in ARTAG.

Another important function of astrocytes is the regulation of water homeostasis through specific water channel aquaporin 4. AQP4 is expressed at the cell membrane of astrocytes, particularly at the perivascular, subpial, and subependymal interfaces (2). Double-labeling immunofluorescence to AQP4 and tau AT8 in samples of the temporal white matter shows AQP4 immunoreactivity in TSAs and in other astrocytes. Due to individual variations we are not able to conclude that AQP4 immunoreactivity is specifically altered in TSAs. However, this does not dismiss the possibility of blood-brain barrier dysfunction in ARTAG as suggested in other studies (33, 35).

The study of the phosphoproteome in relatively pure cases of ARTAG, although limited by the small number of cases, avoids possible contamination of altered tau in ARTAG associated with other tauopathies. Several proteins in ARTAG have differential phosphorylation marks when compared with controls, among them AQP4 at Thr273 and GFAP at positions 8, 14, 82, and 424. GFAP phosphorylation at Ser8 was further validated by immunohistochemistry and immunofluorescence and characterized by confocal microscopy. GFAP is phosphorylated at different sites of the amino-terminal, thus modulating filaments assembly (24, 43, 52). Several kinases phosphorylate GFAP at specific sites; Cdc2 kinase (cyclin dependent kinase 1) phosphorylates GFAP at Ser8 whereas Ca(2+)-CaM-dependent protein kinase II phosphorylates GFAP at Ser13, Ser17, Ser34, and Ser389 (56). The role of cAMP-dependent and Ca²⁺-dependent protein kinases on GFAP phosphorylation has also been studied in digitonin-permeabilized astrocytes exposed to cAMP and Ca²⁺ which increases the phosphorylation state of GFAP (25). Despite these achievements, little is known about the effect of combined phosphorylation at different sites on GFAP filament assembly (52).

Phosphorylation of some aquaporins has been proposed as regulating their water permeability via gating of the channel itself. Certain protein kinases phosphorylate AQP4 thus facilitating AQP4 trafficking and water permeability (20, 26). However, studies in *Xenopus* oocytes have shown that phosphorylation at COOH-terminal residues Ser180, Ser276, Ser285, Ser315, Ser316, Ser321, and Ser322 does not modulate trafficking or channel gating (1, 3, 47). Thus, regulatory patterns and physiological roles for AQP4 remain to be fully explored (2); functional studies are needed to learn about the functional role of AQP4 phosphorylation at Thr273 and its implication in ARTAG.

Phosphoproteomics has also evidenced increased phosphorylation marks in several kinases including calcium/calmodulin-dependent protein kinase type II subunit gamma, cAMP-dependent protein kinase catalytic subunit alpha, c-Jun-amino-terminal kinase-interacting protein 3, cyclin-dependent kinase 12, protein kinase C alpha type, and protein kinase C epsilon type. Since a typical protein kinase must distinguish one from among a few hundred bona fide phosphorylation sites in a background of approximately 700,000 potentially phosphorylatable residues (57), it is premature to advance which are the substrates of such activated kinases in the context of ARTAG. In spite of the large number of putative targets, double-labeling immunofluorescence has shown co-localization of active kinases p38 and PKA α/β with hyperphosphorylated tau in TSAs in ARTAG. Moreover, many other proteins are phosphorylated at specific sites in ARTAG including MAP7 domain-containing protein 1, microtubule-associated protein 1A, microtubule-associated protein 1AA, microtubule-associated protein 1B, microtubule-associated protein 1S, and microtubule-associated protein 2, in addition to microtubule-associated protein tau. Furthermore, increased phosphorylation of microtubule-associated protein 1B, microtubule-associated protein 4, and microtubule-associated protein 6 is found in controls compared with ARTAG. Several neuronal proteins, such as synaptic proteins synapsin-1, synaptophysin, synaptopodin and synaptophilin; and tuberin, are also differentially phosphorylated in ARTAG, indicating that differences in the phosphorylation state of various cytoskeletal and non-cytoskeletal proteins are not limited to astrocytes but also compromise neurons. Little is known about functional implications of tuberin phosphorylation. However, since tuberin is linked to microtubule biology through ROCK2 signaling (15), it can be suggested that changes in tuberin phosphorylation modify microtubule organization.

Several studies in AD have located differentially phosphorylated proteins in the cerebral cortex and hippocampus using bi-dimensional gel electrophoresis and mass spectrometry. Most proteins are linked to energy metabolism, neuronal plasticity, signal transduction, and oxidative stress responses (11, 55, 59). These studies also identify GFAP as a phosphorylated protein in AD. More recently, phosphopeptide enrichment and LC-MS/MS assessment have identified more than one thousand phosphorylated proteins in AD (53). In another study, most of the core phosphoproteins are directly connected and form a functional network linked to synaptic spine formation. Systems biology analyses suggest that over-activated kinases including protein kinases C and calmodulin-dependent kinases initiate synapse pathology (51). The change of the core network starts at a preclinical stage even before histological β -amyloid deposition (51).

The study of Tagawa et al. (51) points to similarities between AD and ARTAG regarding phosphorylation of similar kinases and synaptic proteins. These modifications in AD are independent of β -amyloid and phosphor-tau deposition, and in ARTAG cases independent of neurofibrillary tangle pathology as well. In addition, GFAP phosphorylation is not restricted to ARTAG but also occurs in AD.

The present observations suggest that TSAs are just part of the modifications occurring in ARTAG. TSAs are developed in selected populations of senescent astrocytes in a context of increased protein phosphorylation among which are several kinases with the capacity to phosphorylate a large number of substrates. These observations in several regions not associated with neuronal tau pathology in ARTAG identify changes which are common to AD, and they may explain the frequency of ARTAG in AD and other tauopathies in the elderly.

Finally, the present study shows for the first time the capacity of tau seeding of sarkosyl-insoluble fractions enriched in hyper-phosphorylated tau from selected ARTAG cases in which TSAs are the only source of abnormal hyperphosphorylated tau. Therefore, certain subpopulations of astrocytes may be primary carriers for abnormal tau seeding. Moreover, tau seeding in our model occurred not only in host astrocytes but also in neurons and oligodendroglia, thus pointing out that neurons and oligodendrocytes can be seed targets of astrocyte-derived hyper-phosphorylated tau. This is important, as hyper-phosphorylated tau inclusions are frequent in oligodendrocytes in AGD and in other tauopathies (16, 27). Present observations support the hypothesis that TSAs may facilitate tau hyper-phosphorylation and deposition in neurons and other glial cells in human tauopathies, and they point to the cardinal role of astrocytopathy in the pathogenesis of neurodegenerative diseases with abnormal protein aggregates. The morphology of tau-containing astrocytes after ARTAG inoculation in mice does not have the morphology of TSAs. Its distribution and that of tau-containing neurons and oligodendrocytes in ARTAG-inoculated mice correlate with the inoculation site rather than with the distribution of TSAs in ARTAG. In fact, the same pattern is seen following the inoculation of AD homogenates, in agreement with previous observations with AD extracts (19). Therefore, additional factors must be examined in the future mainly those related with the age of the inoculated animals. ARTAG is a tauopathy related to aging and TSAs are senescent astrocytes. Inoculation of ARTAG (and AD) homogenates in old animals is mandatory to move closer to the environment occurring in old age.

Acknowledgements

We wish to thank the CRG–UPF proteomics unit, and Tom Yohannan for editorial assistance

References

1. Assentoft M, Kaptan S, Fenton RA, Hua SZ, de Groot BL, MacAulay (2013) Phosphorylation of rat aquaporin-4 at Ser(111) is not required for channel gating. *Glia* 61: 1101-1112.
2. Assentoft M, Larsen BR, MacAulay N (2015) Regulation and function of AQP4 in the central nervous system. *Neurochem Res* 40: 2615-2627.
3. Assentoft M, Larsen BR, Olesen ET, Fenton RA, MacAulay N (2014) AQP4 plasma membrane trafficking or channel gating is not significantly modulated by phosphorylation at COOH-terminal serine residues. *Am J Physiol Cell Physiol* 307: C957-65.
4. Boluda S, Iba M, Zhang B, Raible KM, Lee VM, Trojanowski JQ (2015) Differential induction and spread of tau pathology in young PS19 tau transgenic mice following intracerebral injections of pathological tau from Alzheimer's disease or corticobasal degeneration brains. *Acta Neuropathol* 129:221–237.
5. Braak H, Alafuzoff I, Arzberger T, Kretschmar H, Del Tredici K. Staging of Alzheimer disease-associated neurofibrillary pathology using paraffin sections and immunocytochemistry. *Acta Neuropathol* 2006; 112: 389-404.
6. Braak H, Braak E (1991) Neuropathological staging of Alzheimer-related changes. *Acta Neuropathol* 82: 239-259.
7. Clavaguera F, Bolmont T, Crowther RA, Abramowski D, Frank S, Probst A, Fraser G, Stalder AK, Beibel M, Staufenbiel M, Jucker M, Goedert M, Tolnay M (2009) Transmission and spreading of tauopathy in transgenic mouse brain. *Nat Cell Biol* 11:909-913.
8. Clavaguera F, Lavenir I, Falcon B, Frank S, Goedert M, Tolnay M (2013) "Prion-like" templated misfolding in tauopathies. *Brain Pathol* 23:342–349
9. Crary JF, Trojanowski JQ, Schneider JA, Abisambra JF, Abner EL, Alafuzoff I, Arnold SE, Attems J, Beach TG, Bigio EH, Cairns NJ, Dickson DW, Gearing M, Grinberg LT, Hof PR, Hyman BT, Jellinger K, Jicha GA, Kovacs GG, Knopman DS,

Kofler J, Kukull WA, Mackenzie IR, Masliah E, McKee A, Montine TJ, Murray ME, Neltner JH, Santa-Maria I, Seeley WW, Serrano-Pozo A, Shelanski ML, Stein T, Takao M, Thal DR, Toledo JB, Troncoso JC, Vonsattel JP, White CL 3rd, Wisniewski T, Woltjer RL, Yamada M, Nelson PT (2014) Primary age-related tauopathy (PART): a common pathology associated with human aging. *Acta Neuropathol* 128: 755-766.

10. Dabir DV, Robinson MB, Swanson E, Zhang B, Trojanowski JQ, Lee VM, Forman MS (2006) Impaired glutamate transport in a mouse model of tau pathology in astrocytes. *J Neurosci* 26: 644-654.

11. Di Domenico F, Sultana R, Barone E, Perluigi M, Cini C, Mancuso C, Cai J, Pierce WM, Butterfield DA (2011) Quantitative proteomics analysis of phosphorylated proteins in the hippocampus of Alzheimer's disease subjects. *J Proteomics* 74: 1091-1103.

12. Ferrer I (2017) Diversity of astroglial responses across human neurodegenerative disorders and brain aging. *Brain Pathol* 27: 645–674.

13. Ferrer I, Legati A, García-Monco JC, Gomez-Beldarrain M, Carmona M, Blanco R, Seeley WW, Coppola G (2015) Familial behavioral variant frontotemporal dementia associated with astrocyte-predominant tauopathy. *J Neuropathol Exp Neurol* 74: 370-379.

14. Ferrer I, López-González I, Carmona M, Arregui L, Dalfó E, Torrejón-Escribano B, Diehl R, Kovacs GG (2013) Glial and neuronal tau pathology in tauopathies: characterization of disease-specific phenotypes and tau pathology progression. *J Neuropathol Exp Neurol* 73: 81-97

15. Ferrer I, Mohan P, Chen H, Castellsague J, Gómez-Baldó L, Carmona M, García N, Aguilar H, Jiang J, Skowron M, Nellist M, Ampuero I, Russi A, Lázaro C, Maxwell CA, Pujana MA (2014) Tubers from patients with tuberous sclerosis complex are characterized by changes in microtubule biology through ROCK2 signalling. *J Pathol* 233: 247-257.

16. Ferrer I, Santpere G, van Leeuwen FW (2008) Argyrophilic grain disease. *Brain* 146: 1640-1651.

17. Forman MS, Lal D, Zhang B, Dabir DV, Swanson E, Lee VM, Trojanowski JQ (2005) Transgenic mouse model of tau pathology in astrocytes leading to nervous system degeneration. *J Neurosci* 25: 3539-3550.
18. García-Matas S, Gutierrez-Cuesta J, Coto-Montes A, Rubio-Acero R, Díez-Vives C, Camins A, Pallàs M, Sanfeliu C, Cristòfol R (2008) Dysfunction of astrocytes in senescence-accelerated mice SAMP8 reduces their neuroprotective capacity. *Aging Cell* 7: 630-640.
19. Guo JL, Narasimhan S, Changolkar L, He Z, Stieber A, Zhang B, Gathagan RJ, Iba M, McBride JD, Trojanowski JQ, Lee VMY (2016) Unique pathological tau conformers from Alzheimer's brains transmit tau pathology in nontransgenic mice. *J Exp Med* 213: 2635-2654.
20. Han Z, Wax MB, Patil RV (1998) Regulation of aquaporin-4 water channels by phorbol ester-dependent protein phosphorylation. *J Biol Chem* 273: 6001-6004.
21. Hashimoto N, Takeuchi T, Ishihara R, Ukai K, Kobayashi H, Iwata K, Mizuno Y, Yamaguchi H, Shibayama H (2003) Glial fibrillary tangles in diffuse neurofibrillary tangles with calcification. *Acta Neuropathol* 106: 150-156.
22. Ikeda K, Akiyama H, Arai T, Nishimura T (1998) Glial tau pathology in neurodegenerative diseases: their nature and comparison with neuronal tangles. *Neurobiol Aging* 19 Suppl: S85-91.
23. Ikeda K, Akiyama H, Kondo H, Haga C, Tanno E, Tokuda T, Ikeda S (1995) Thorn-shaped astrocytes: possibly secondarily induced tau-positive glial fibrillary tangles. *Acta Neuropathol* 90: 620-625.
24. Inagaki M, Nakamura Y, Takeda M, Nishimura T, Inagaki N (1994) Glial fibrillary acidic protein: dynamic property and regulation by phosphorylation. *Brain Pathol* 4: 239-243.
25. Karla J, Goofried C, Tramontina F, Dunkley P, Rodnighta R, Gonçalves CA (2000) GFAP phosphorylation studied in digitonin-permeabilized astrocytes: standardization of conditions. *Brain Res* 853: 32-40.

26. Kitchen P, Day RE, Taylor LH, Salman MM, Bill RM, Conner MT (2015) Identification and molecular mechanisms of the rapid tonicity-induced relocalization of the aquaporin 4 channel. *J Biol Chem* 290: 16873-16881.
27. Kovacs GG (2015) Invited review: Neuropathology of tauopathies: principles and practice. *Neuropathol Appl Neurobiol* 41: 3-23.
28. Kovacs GG, Ferrer I, Grinberg LT, Alafuzoff I, Attems J, Budka H, Cairns NJ, Crary JF, Duyckaerts C, Ghetti B, Halliday GM, Ironside JW, Love S, Mackenzie IR, Munoz DG, Murray ME, Nelson PT, Takahashi H, Trojanowski JQ, Ansorge O, Arzberger T, Baborie A, Beach TG, Bieniek KF, Bigio EH, Bodi I, Dugger BN, Feany M, Gelpi E, Gentleman SM, Giaccone G, Hatanpaa KJ, Heale R, Hof PR, Hofer M, Hortobágyi T, Jellinger K, Jicha GA, Ince P, Kofler J, Kövari E, Kril JJ, Mann DM, Matej R, McKee AC, McLean C, Milenkovic I, Montine TJ, Murayama S, Lee EB, Rahimi J, Rodriguez RD, Rozemüller A, Schneider JA, Schultz C, Seeley W, Seilhean D, Smith C, Tagliavini F, Takao M, Thal DR, Toledo JB, Tolnay M, Troncoso JC, Vinters HV, Weis S, Wharton SB, White CL 3rd, Wisniewski T, Woulfe JM, Yamada M, Dickson DW (2016) Aging-related tau astroglialopathy (ARTAG): harmonized evaluation strategy. *Acta Neuropathol* 131: 87-102.
29. Kovacs GG, Lee VM, Trojanowski JQ (2017) Protein astroglialopathies in human neurodegenerative diseases and aging. *Brain Pathol* 27: 675-690.
30. Kovacs GG, Molnár K, László L, Ströbel T, Botond G, Hönigschnabl S, Reiner-Concin A, Palkovits M, Fischer P, Budka H (2011) A peculiar constellation of tau pathology defines a subset of dementia in the elderly. *Acta Neuropathol* 122: 205-222.
31. Kovacs GG, Robinson JL, Xie SX, Lee EB, Grossman M, Wolk DA, Irwin DJ, Weintraub D, Kim CF, Schuck T, Yousef A, Wagner ST, Suh E, Van Deerlin VM, Lee VM, Trojanowski JQ (2017) Evaluating the patterns of aging-related tau astroglialopathy unravels novel insights into brain aging and neurodegenerative diseases. *J Neuropathol Exp Neurol* 76: 270-288.
32. Kovacs GG, Xie SX, Lee EB, Robinson JL, Caswell C, Irwin DJ, Toledo JB, Johnson VE, Smith DH, Alafuzoff I, Attems J, Bencze J, Bieniek KF, Bigio EH, Bodi I, Budka H, Dickson DW, Dugger BN, Duyckaerts C, Ferrer I, Forrest SL, Gelpi E, Gentleman SM, Giaccone G, Grinberg LT, Halliday GM, Hatanpaa KJ, Hof PR, Hofer

M, Hortobágyi T, Ironside JW, King A, Kofler J, Kövari E, Kril JJ, Love S, Mackenzie IR, Mao Q, Matej R, McLean C, Munoz DG, Murray ME, Neltner J, Nelson PT, Ritchie D, Rodriguez RD, Rohan Z, Rozemuller A, Sakai K, Schultz C, Seilhean D, Smith V, Tacik P, Takahashi H, Takao M, Rudolf Thal D, Weis S, Wharton SB, White CL 3rd, Woulfe JM, Yamada M, Trojanowski JQ (2017) Multiple assessment of aging-related astroglial pathology. *J Neuropathol Exp Neurol* 76: 605-619.

33. Kovacs GC, Yousef A, Kaindl S, Lee VM, Trojanowski JQ (2017) Connexin -43 and aquaporin-4 are markers of ageing-related tau astroglial pathology (ARTAG)-related astroglial response. *Neuropathol Appl Neurobiol* Jul 29. Doi: 10.1111/nan.12427 [Epub ahead of print]

34. Lewis J, Dickson DW (2016) Propagation of tau pathology: hypotheses, discoveries, and yet unresolved questions from experimental and human brain studies. *Acta Neuropathol* 131: 27-48.

35. Ling H, Neal JW, Revesz T (2017) Evolving concepts of chronic traumatic encephalopathy as a neuropathological entity. *Neuropathol Appl Neurobiol* 43: 467-476.

36. Liu AKL, Goldfinger MH, Questari HE, Pearce RKB, Gentleman SM (2016) ARTAG in the basal forebrain: widening the constellation of astrocytic tau pathology. *Acta Neuropathol Commun* 4: 59.

37. López-González I, Carmona M, Blanco R, Luna-Muñoz J, Martínez-Mandonado A, Mena R, Ferrer I (2013) Characterization of thorn-shaped astrocytes in white matter of temporal lobe in Alzheimer's disease brains. *Brain Pathol* 23:144-153.

38. Llorens F, Thüne K, Tahir W, Kanata E, Diaz-Lucena D, Xanthopoulos K, Kovatsi E, Pleschka C, Garcia-Esparcia P, Schmitz M, Ozbay D, Correia S, Correia Â, Milosevic I, Andréoletti O, Fernández-Borges N, Vorberg IM, Glatzel M, Sklaviadis T, Torres JM, Krasemann S, Sánchez-Valle R, Ferrer I, Zerr I (2017) YKL-40 in the brain and cerebrospinal fluid of neurodegenerative dementias. *Mol Neurodegener* 12: 83.

39. Maragakis NJ, Rothstein JD (2006) Mechanisms of disease: astrocytes in neurodegenerative disease. *Nat Clin Pract Neurol* 2: 679-689.

40. Muñoz DG, Woulfe J, Kertesz A (2007) Argyrophilic thorny astrocyte clusters in association with Alzheimer's disease pathology in possible primary progressive aphasia. *Acta Neuropathol* 114: 347-357.
41. Narasimhan S, Guo JL, Changolkar L, Stieber A, McBride JD, Silva LV, He Z, Zhang B, Gathagan RJ, Trojanowski JQ, Lee VMY (2017) Pathological tau strains from human brains recapitulate the diversity of tauopathies in non-transgenic mouse brain. *J Neurosci* 37: 11406-11423.
42. Nedergaard M, Takano T, Hansen AJ (2002) Beyond the role of glutamate as a neurotransmitter. *Nat Rev Neurosci* 3: 748-755.
43. Noetzel MJ (1990) Phosphorylation of the glial fibrillary acidic protein. *J Neurosci Res* 27: 184-192.
44. Osborn LM, Kamphuis W, Wadman WJ, Hol EM (2016) Astrogliosis: an integral player in the pathogenesis of Alzheimer's disease. *Prog Neurobiol* 144:121–141.
45. Pekny M, Pekna M, Messing A, Steinhäuser C, Lee JM, Parpura V, Hol M, Sofroniew MW, Verkhratsky A (2016) Astrocytes: a central element in neurological diseases. *Acta Neuropathol* 131:323–345.
46. Rodríguez JJ, Yeh CY, Terzieva S, Olabarria M, Kulijewicz-Nawrot M, Verkhratsky A (2014) Complex and region-specific changes in astroglial markers in the aging brain. *Neurobiol Aging* 35: 15-23.
47. Sachdeva R, Singh B (2014) Phosphorylation of Ser-180 of rat aquaporin-4 shows marginal affect on regulation of water permeability: molecular dynamics study. *J Biomol Struct Dyn* 32: 555-566.
48. Salminen A, Ojala J, Kaarniranta K, Haapasalo A, Hiltunen M, Soininen H (2011) Astrocytes in the aging brain express characteristics of senescence-associated secretory phenotype. *Eur J Neurosci* 34: 3-11.
49. Schultz C, Ghebremedhin E, Del Tredici K, Rüb U, Braak H (2004) High prevalence of thorn-shaped astrocytes in the aged human medial temporal lobe. *Neurobiol Aging* 25: 397-405.

50. Schwartz D, Gygi SP (2005) An iterative statistical approach to the identification of the protein phosphorylation motifs from large-scale data sets. *Nature Biotech* 23: 1391-1398.

51. Tagawa K, Homma H, Saito A, Fujita K, Chen X, Imoto S, Oka T, Ito H, Motoki K, Yoshida C, Hatsuta H, Murayama S, Iwatsubo T, Miyano S, Okazawa H (2015) Comprehensive phosphoproteome analysis unravels the core signaling network that initiates the earliest synapse pathology in preclinical Alzheimer's disease brain. *Hum Mol Genet* 24: 540-558.

52. Takemura M, Gomi H, Colucci-Guyon E, Itohara S (2002) Protective role of phosphorylation in turnover of glial fibrillary acidic protein in mice. *J Neurosci* 22: 6972-6979.

53. Tan H, Wu Z, Wang H, Bai B, Li Y, Wang X, Zhai B, Beach TG, Peng J (2015) Refined phosphopeptide enrichment by phosphate additive and the analysis of human brain phosphoproteome. *Proteomics* 15: 500-507.

54. Tolnay M, Braak H (2011) Argyrophilic grain disease. In: *Neurodegeneration, the Molecular Pathology of Dementia and Molecular Disorders*, Dickson DW, Weller RO (eds.), pp. 165-170, Wiley-Blackwell, Oxford.

55. Triplett JC, Swomley AM, Cai J, Klein JB, Butterfield DA (2016) Quantitative phosphoproteomic analyses of the inferior parietal lobule from three different pathological stages of Alzheimer's disease. *J Alzheimers Dis* 49: 45-62.

56. Tsujimura K, Tanaka J, Ando S, Matsuoka Y, Kusubata M, Sugiura H, Yamauchi T, Inagaki M (1994) Identification of phosphorylation sites on glial fibrillary acidic protein for cdc2 kinase and Ca(2+)-calmodulin-dependent protein kinase II. *J Biochem* 116: 426-434.

57. Ubersax JA, Ferrell JE (2007) Mechanisms of specificity in protein phosphorylation. *Nature Rev Mol Cell Biol* 8: 530-541.

58. Verkhratsky A, Rodriguez JJ, Parpura V (2014) Neuroglia in ageing and disease. *Cell Tissue Res* 357:493–503.

59. Zahid S, Oellerich M, Asif AR, Ahmed N (2012) Phosphoproteome profiling of substantia nigra and cortex regions of Alzheimer's disease patients. *J Neurochem* 121: 954-963.

Table I: Antibodies used, origins, dilutions, and suppliers

Table II: Cases and distribution of lesions in the present series of pure ARTAG

Table III: Total list of differentially phosphorylated proteins in ARTAG compared with controls, and in controls compared with ARTAG

Table IV: List of phosphorylated proteins in ARTAG and identification of phosphorylation sites (probability site value, pRS, greater than 75% is highlighted in yellow)

Supplementary Table 1: Whole data of one-hundred twenty-two differentially occupied phosphosites differentially expressed in ARTAG compared with controls, and 36 phosphosites differentially occupied in controls when compared with ARTAG

Figure legends

Figure 1: A-L: single immunohistochemistry with anti-tau antibodies directed to N-terminal, middle, and C-terminal regions of tau. A, D, G, J: subependymal astrocytes; B, E, H, K: subpial astrocytes; C, F, I, L: temporal white matter. A-C: antibody 499 (amino acids 14-26; amino terminal); D-F: antibody 229 (amino acids 229-233, middle region); G-I: antibody 394 (amino acids 394-398, C-terminal); J-L: antibody tau-100 (P-tau Thr212-Ser214). TSAs are stained with all these antibodies. Paraffin sections slightly counterstained with haematoxylin; A-I, bar in I = 25µm; J-L, bar in L = 100µm. M, N: double-labeling immunofluorescence and confocal microscopy using (M) antibody 499 (green) and P-tau Thr181 (red); and (N) antibody 394 (green) and P-tau Thr181 (red) in the vicinity of a blood vessel (M, asterisk) and in the temporal white matter. N-terminal and C-terminal tau segments are co-expressed with phosphorylated tau. Paraffin sections; nuclei (blue) are stained with DRAQ5TM; M, bar = 75µm; N, bar = 40µm.

Figure 2: GFAP-immunoreactive astrocytes in white matter (A-D) (A) and ARTAG cases in TSAs-rich regions (B) and neighboring regions without TSAs astrocytes (C). GFAP-positive astrocytes in ARTAG regions without TSAs have larger branches when compared with controls. However, THAs have smaller size and reduced number of branches when compared with astrocytes in controls. Paraffin sections; nuclei (blue) are stained with DRAQ5TM; bar = 50µm. Particle selection mascara of astrocytes is shown in white matter (D). Quantification of astrocytes areas per µm² (left lower panels) and astrocyte average size (right lower panels). Graphs show mean ± SEM of three different sections. Quantifications analyzed by One-way ANOVA show significant difference among groups * $p < 0.05$ in white matter astrocyte coverage area; Turkey post-hoc shows significant differences # $p < 0.05$ in astrocyte coverage area between THAs (P-tau+) and neighboring P-tau negative (P-tau-) astrocytes in ARTAG.

Figure 3: Double-labeling immunofluorescence to GFAP (green) and AT8 (red) showing the morphology of TSAs in the temporal white matter. Short arrow: cells only stained green; arrowhead: cells only stained red. Hyper-phosphorylated tau-containing astrocytes have reduced GFAP immunoreactivity. Paraffin sections; nuclei (blue) are stained with DRAQ5TM; bar = 50µm.

Figure 4: A: Double-labeling immunofluorescence to YKL-40 (green) and AT8 (red) in one cluster of TSAs in temporal white matter. B: Double-labeling immunofluorescence

to vimentin (green) and AT8 (red) in temporal white matter. Note decreased YKL-40 and vimentin immunoreactivity in TSAs. Long arrow: cells with double staining; short arrow: cells only stained green; arrowhead: cells only stained red. Paraffin sections, nuclei stained with DRAQ5TM (blue); bar = 50µm.

Figure 5: Gel electrophoresis and western blotting of sarkosyl-insoluble fractions from frontal cortex of Alzheimer disease stage V (ADV) processed in parallel with ARTAG; upper panel, basal forebrain; lower panel medulla oblongata. Three phospho-tau bands (antibody P-tau Ser422) of 68kDa, 64kDa, and 60kDa; several bands of molecular weight between 50kDa and 30kDa, and a lower band of about 23kDa are seen in AD. These correspond to two bands of 4R tau between 68 and 60kDa and several bands of lower molecular stained visualized with specific anti-4R antibodies. In contrast, two bands of 68kDa and 64kDa, and several bands of lower molecular weight corresponding to truncated forms of tau are seen in ARTAG. The lower phospho-tau band of about 23kDa is absent in ARTAG. Curiously, a very weak band of 68kDa and a weak double-band at 64 kDa are seen in medulla oblongata. Parallel membranes blotted with 4Rtau antibodies show a doublet of 64 kDa.

Figure 6: Double-labeling immunofluorescence to SOD2 (green) and hyper-phosphorylated tau (clone AT8: red) (A), AQP4 (green), and tau AT8 (red) (B) in the temporal white matter, and GLT-1 (green) and hyper-phosphorylated tau (clone AT8: red) in the subpial region at the level of the medulla oblongata (C). TSAs and non-TSAs are equally immunoreactive to SOD2. TSAs, like other astrocytes in the temporal white matter, exhibit low AQP4 immunoreactivity which is displaced to the periphery by tau deposits. TSAs have GLT-1 immunoreactivity at the cell membrane. Long arrow: cells with double staining; short arrow: cells only stained green; arrowhead: cells only stained red. Paraffin sections, nuclei (blue) are stained with DRAQ5TM, A-F, bar = 40µm; G-I, bar = 10µm.

Figure 7: A: Heat map of phosphosites in control (CC) and ARTAG (AG) cases showing differences between the two groups. **B:** Phosphomotif enrichment analysis reveals the motif SP enriched in the ARTAG samples. The SP site is a phosphorylation site used for a wide number of kinases such as MAPKs (including p38) and CDKs.

Figure 8: Double-labeling immunofluorescence with antibodies against GFAP-P and tau Thr181 (A), anti-PKA-P (B), anti-p38-P (C), and anti-tuberin-P (D) and AT8 in ARTAG. TSAs contain GFAP-P, PKA-P, and p38-P but not tuberin-P. GFAP-P is

expressed in hyper-phosphorylated tau-bearing and non-hyper-phosphorylated tau-bearing astrocytes in the temporal white matter. Tuberin-P is expressed in neurons of the hippocampus but not in tau-containing astrocytes. Long arrow: cells with double staining; short arrow: cells only stained green; arrowhead: cells only stained red. Paraffin sections; nuclei (blue) are stained with DRAQ5TM; bar = 40µm.

Figure 9: Hyper-phosphorylated tau containing cells following intra-hippocampal inoculation of sarkosyl-insoluble fractions from ARTAG cases to WT mice. A, B: inoculated at 7 months and killed at the age of 10 months; C-L: inoculated at 3 months and killed at the age of 10 months. A, C: fimbria; B: hippocampus; D-F, I: corpus callosum; J, K: CA1 region of the hippocampus; H: subiculum; G-L: dentate gyrus. A-I: antibody tau AT8; J: anti-4Rtau; K, L: anti-3Rtau. Paraffin sections slightly counterstained with haematoxylin; A-L, excepting D, bar in L = 25µm; D, bar = 100µm.

Figure 10: WT mice inoculated with ARTAG in the hippocampus at the age of 7 months and killed at the age of 10 months. A: Double-labeling immunofluorescence to NeuN (green) and P-tau Thr181 (red). B: Double-labeling immunofluorescence to GFAP (green) and AT8 (red). C: Double-labeling immunofluorescence to Iba-1 (green) and AT8 (red). Subpopulations of neurons and astrocytes, but not microglia, contain hyper-phosphorylated tau. Paraffin sections, nuclei stained with DRAQ5TM (blue). Long arrow: cells with double staining; short arrow: cells only stained green; arrowhead: cells only stained red. A, bar = 30µm; B, bar = 20µm; C, bar = 50µm.

Figure 11: WT mice inoculated with ARTAG in the hippocampus at the age of 3 months and killed at the age of 10 months. A: Double-labeling immunofluorescence to NeuN (green) and tauThr181 (red). B: Double-labeling immunofluorescence to phosphorylated p38 Thr180-Tyr182 (green) and AT8 (red). C, D: Double-labeling immunofluorescence to GFAP (green) and AT8 (red). E, F: Double-labeling immunofluorescence to Iba-1 (green) and AT8 (red). G, H: Double-labeling immunofluorescence to Olig2 (green) and AT8 (red). Subpopulations of neurons (A, B), astrocytes (C, D) and oligodendrocytes (G, H) contain hyper-phosphorylated tau. Hippocampal neurons containing hyper-phosphorylated tau co-express active tau kinase p38. Long arrow: cells with double staining; short arrow: cells only stained green; arrowhead: cells only stained red. Paraffin sections, nuclei stained with DRAQ5TM (blue); bar = 25µm.

Supplementary Figure 1: mRNA expression levels of 3R tau and 4R tau in the temporal white matter in middle-aged (MA) control cases, Alzheimer's disease (AD) and ARTAG cases (**A**), and 3Rtau/4Rtau mRNA ration in every group (**B**). No significant differences are observed at mRNA level, but a tendency to decreased 3Rtau and 4Rtau mRNA, and reduced 3R/4R ratio is found in AD and ARTAG compared with controls.

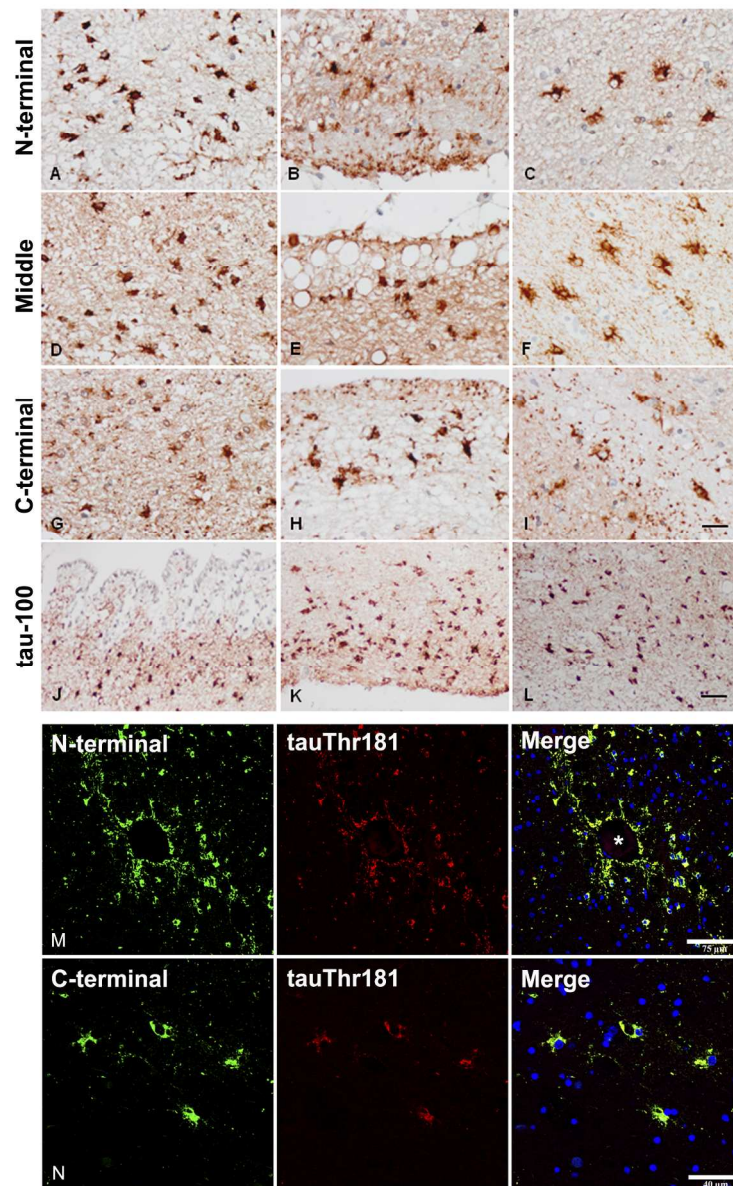


Figure 1: A-L: single immunohistochemistry with anti-tau antibodies directed to N-terminal, middle, and C-terminal regions of tau. A, D, G, J: subependymal astrocytes; B, E, H, K: subpial astrocytes; C, F, I, L: temporal white matter. A-C: antibody 499 (amino acids 14-26; amino terminal); D-F: antibody 229 (amino acids 229-233, middle region); G-I: antibody 394 (amino acids 394-398, C-terminal); J-L: antibody tau-100 (P-tau Thr212-Ser214). TSAs are stained with all these antibodies. Paraffin sections slightly counterstained with haematoxylin; A-I, bar in I = 25µm; J-L, bar in L = 100µm. M, N: double-labeling immunofluorescence and confocal microscopy using (M) antibody 499 (green) and P-tau Thr181 (red); and (N) antibody 394 (green) and P-tau Thr181 (red) in the vicinity of a blood vessel (M, asterisk) and in the temporal white matter. N-terminal and C-terminal tau segments are co-expressed with phosphorylated tau. Paraffin sections; nuclei (blue) are stained with DRAQ5TM; M, bar = 75µm; N, bar = 40µm.

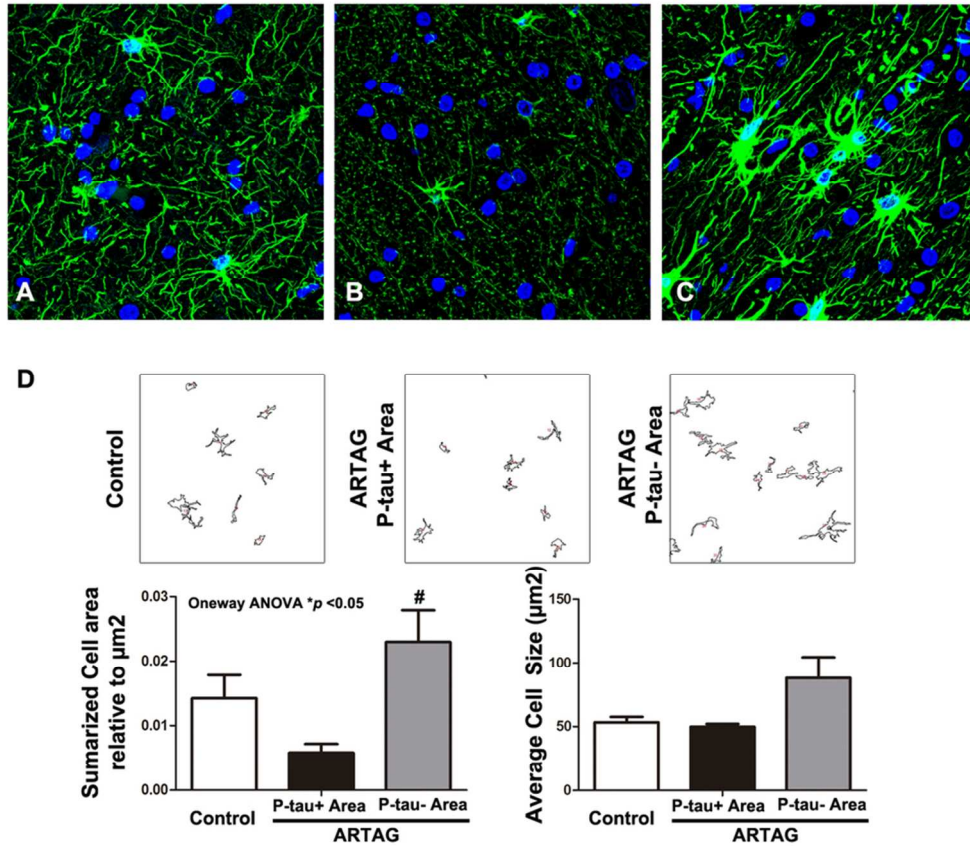


Figure 2: GFAP-immunoreactive astrocytes in white matter (A-D) (A) and ARTAG cases in TSAs-rich regions (B) and neighboring regions without TSAs astrocytes (C). GFAP-positive astrocytes in ARTAG regions without TSAs have larger branches when compared with controls. However, THAs have smaller size and reduced number of branches when compared with astrocytes in controls. Paraffin sections; nuclei (blue) are stained with DRAQ5 TM; bar = 50 μm . Particle selection mascara of astrocytes is shown in white matter (D). Quantification of astrocytes areas per μm^2 (left lower panels) and astrocyte average size (right lower panels). Graphs show mean \pm SEM of three different sections. Quantifications analyzed by One-way ANOVA show significant difference among groups * $p < 0.05$ in white matter astrocyte coverage area; Turkey post-hoc shows significant differences # $p < 0.05$ in astrocyte coverage area between THAs (P-tau+) and neighboring P-tau negative (P-tau-) astrocytes in ARTAG.

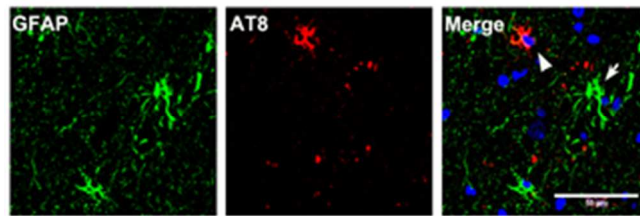


Figure 3: Double-labeling immunofluorescence to GFAP (green) and AT8 (red) showing the morphology of TSAs in the temporal white matter. Short arrow: cells only stained green; arrowhead: cells only stained red. Hyper-phosphorylated tau-containing astrocytes have reduced GFAP immunoreactivity. Paraffin sections; nuclei (blue) are stained with DRAQ5™; bar = 50µm.

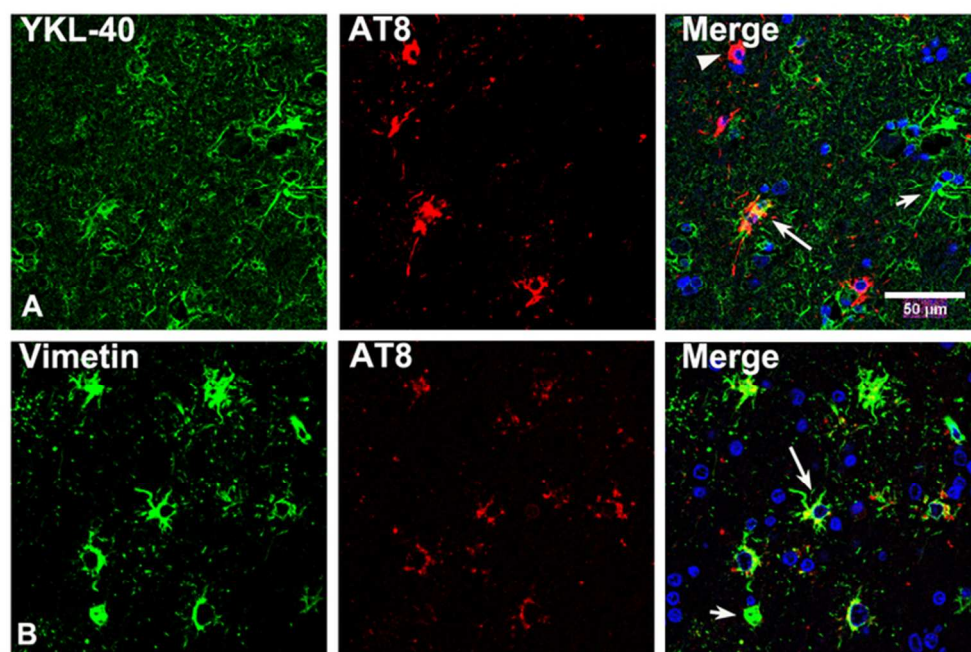


Figure 4: A: Double-labeling immunofluorescence to YKL-40 (green) and AT8 (red) in one cluster of TSAs in temporal white matter. B: Double-labeling immunofluorescence to vimentin (green) and AT8 (red) in temporal white matter. Note decreased YKL-40 and vimentin immunoreactivity in TSAs. Long arrow: cells with double staining; short arrow: cells only stained green; arrowhead: cells only stained red. Paraffin sections, nuclei stained with DRAQ5™ (blue); bar = 50μm.

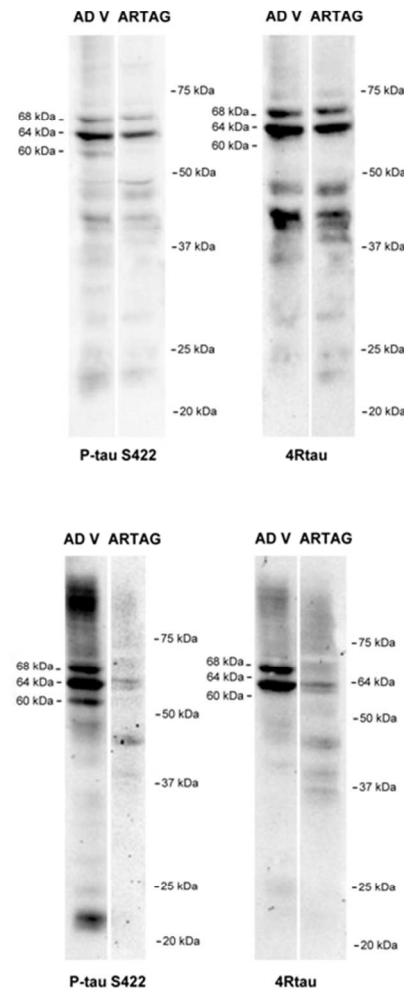


Figure 5: Gel electrophoresis and western blotting of sarkosyl-insoluble fractions from frontal cortex of Alzheimer disease stage V (ADV) processed in parallel with ARTAG; upper panel, basal forebrain; lower panel medulla oblongata. Three phospho-tau bands (antibody P-tau Ser422) of 68kDa, 64kDa, and 60kDa; several bands of molecular weight between 50kDa and 30kDa, and a lower band of about 23kDa are seen in AD. These correspond to two bands of 4R tau between 68 and 60kDa and several bands of lower molecular weight stained visualized with specific anti-4R antibodies. In contrast, two bands of 68kDa and 64kDa, and several bands of lower molecular weight corresponding to truncated forms of tau are seen in ARTAG. The lower phospho-tau band of about 23kDa is absent in ARTAG. Curiously, a very weak band of 68kDa and a weak double-band at 64 kDa are seen in medulla oblongata. Parallel membranes blotted with 4Rtau antibodies show a doublet of 64 kDa.

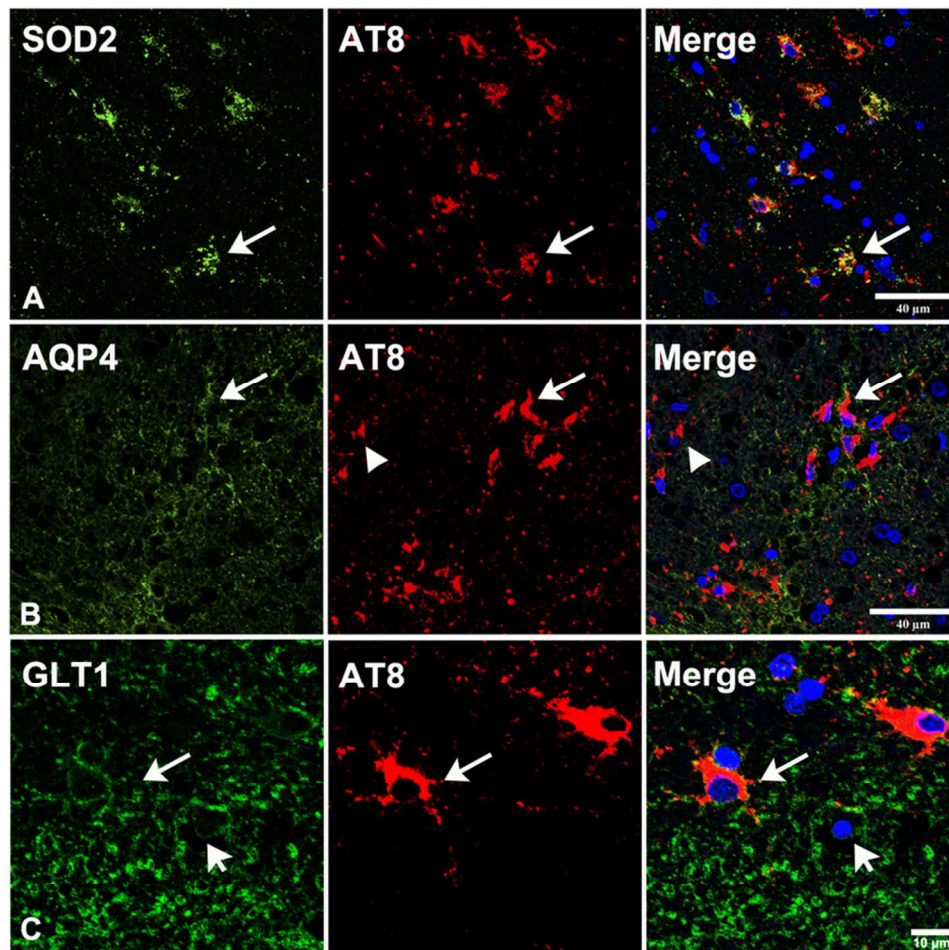


Figure 6: Double-labeling immunofluorescence to SOD2 (green) and hyper-phosphorylated tau (clone AT8: red) (A), AQP4 (green), and tau AT8 (red) (B) in the temporal white matter, and GLT-1 (green) and hyper-phosphorylated tau (clone AT8: red) in the subpial region at the level of the medulla oblongata (C). TSAs and non-TSAs are equally immunoreactive to SOD2. TSAs, like other astrocytes in the temporal white matter, exhibit low AQP4 immunoreactivity which is displaced to the periphery by tau deposits. TSAs have GLT-1 immunoreactivity at the cell membrane. Long arrow: cells with double staining; short arrow: cells only stained green; arrowhead: cells only stained red. Paraffin sections, nuclei (blue) are stained with DRAQ5™, A-F, bar = 40μm; G-I, bar = 10μm.

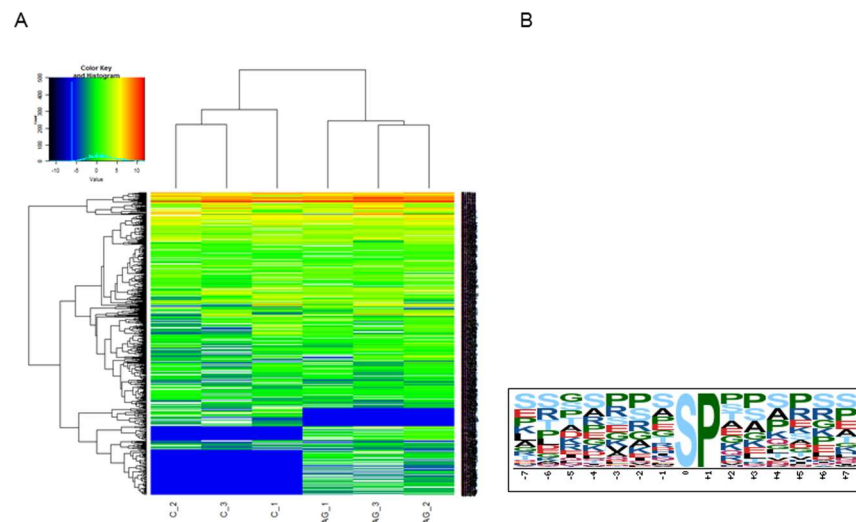


Figure 7: A: Heat map of phosphosites in control (CC) and ARTAG (AG) cases showing differences between the two groups. B: Phosphomotif enrichment analysis reveals the motif SP enriched in the ARTAG samples. The SP site is a phosphorylation site used for a wide number of kinases such as MAPKs (including p38) and CDKs.

Accep

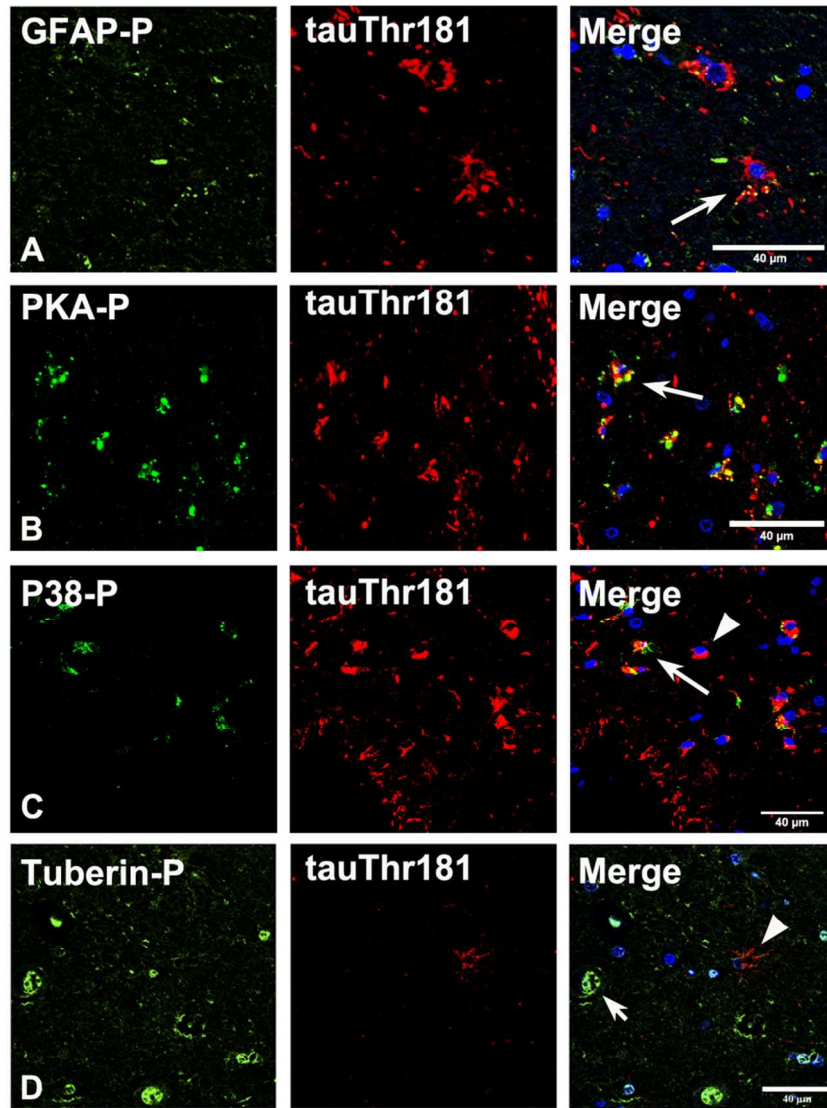


Figure 8: Double-labeling immunofluorescence with antibodies against GFAP-P and tau Thr181 (A), anti-PKA-P (B), anti-p38-P (C), and anti-tuberin-P (D) and AT8 in ARTAG. TSAs contain GFAP-P, PKA-P, and p38-P but not tuberin-P. GFAP-P is expressed in hyper-phosphorylated tau-bearing and non-hyper-phosphorylated tau-bearing astrocytes in the temporal white matter. Tuberin-P is expressed in neurons of the hippocampus but not in tau-containing astrocytes. Long arrow: cells with double staining; short arrow: cells only stained green; arrowhead: cells only stained red. Paraffin sections; nuclei (blue) are stained with DRAQ5™; bar = 40μm.

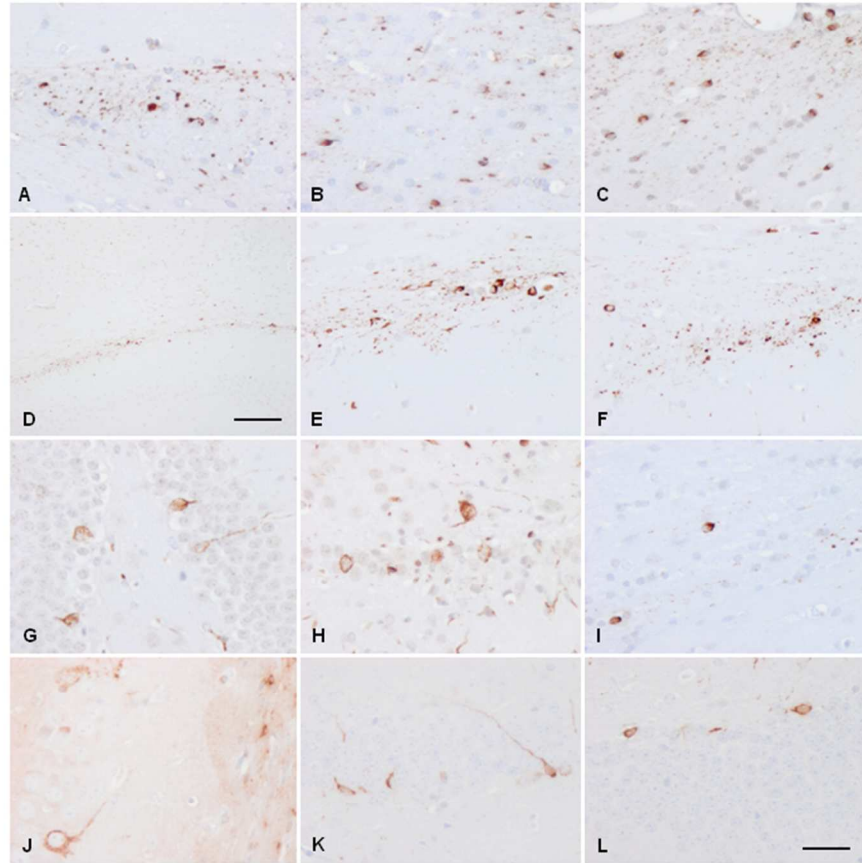


Figure 9: Hyper-phosphorylated tau containing cells following intra-hippocampal inoculation of sarkosyl-insoluble fractions from ARTAG cases to WT mice. A, B: inoculated at 7 months and killed at the age of 10 months; C-L: inoculated at 3 months and killed at the age of 10 months. A, C: fimbria; B: hippocampus; D-F, I: corpus callosum; J, K: CA1 region of the hippocampus; H: subiculum; G-L: dentate gyrus. A-I: antibody tau AT8; J: anti-4Rtau; K, L: anti-3Rtau. Paraffin sections slightly counterstained with haematoxylin; A-L, excepting D, bar in L = 25µm; D, bar = 100µm.

Figure 9: Hyper-phosphorylated tau containing cells following intra-hippocampal inoculation of sarkosyl-insoluble fractions from ARTAG cases to WT mice. A, B: inoculated at 7 months and killed at the age of 10 months; C-L: inoculated at 3 months and killed at the age of 10 months. A, C: fimbria; B: hippocampus; D-F, I: corpus callosum; J, K: CA1 region of the hippocampus; H: subiculum; G-L: dentate gyrus. A-I: antibody tau AT8; J: anti-4Rtau; K, L: anti-3Rtau. Paraffin sections slightly counterstained with haematoxylin; A-L, excepting D, bar in L = 25µm; D, bar = 100µm.

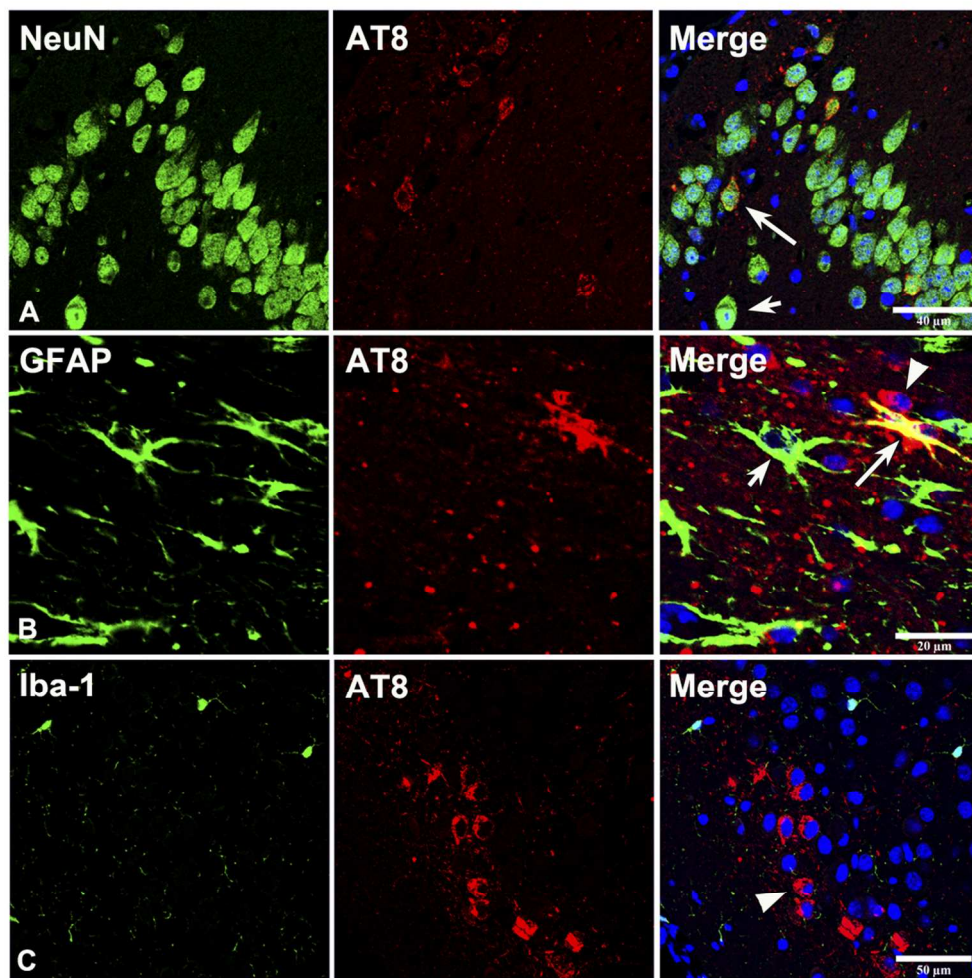


Figure 10: WT mice inoculated with ARTAG in the hippocampus at the age of 7 months and killed at the age of 10 months. A: Double-labeling immunofluorescence to NeuN (green) and P-tau Thr181 (red). B: Double-labeling immunofluorescence to GFAP (green) and AT8 (red). C: Double-labeling immunofluorescence to Iba-1 (green) and AT8 (red). Subpopulations of neurons and astrocytes, but not microglia, contain hyper-phosphorylated tau. Paraffin sections, nuclei stained with DRAQ5TM (blue). Long arrow: cells with double staining; short arrow: cells only stained green; arrowhead: cells only stained red. A, bar = 30µm; B, bar = 20µm; C, bar = 50µm.

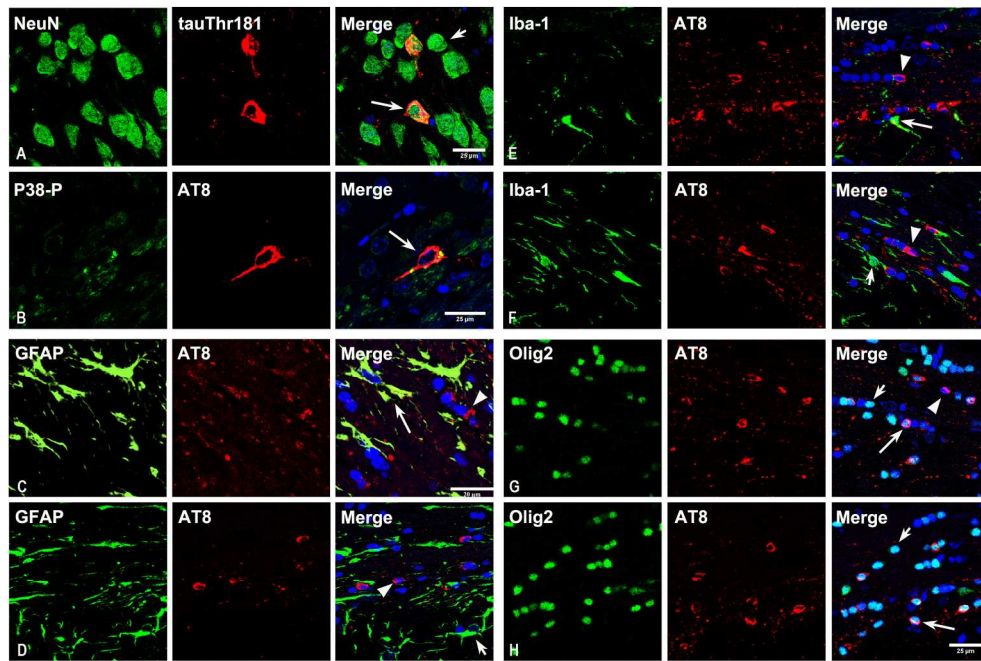


Figure 11: WT mice inoculated with ARTAG in the hippocampus at the age of 3 months and killed at the age of 10 months. A: Double-labeling immunofluorescence to NeuN (green) and tauThr181 (red). B: Double-labeling immunofluorescence to phosphorylated p38 Thr180-Tyr182 (green) and AT8 (red). C, D: Double-labeling immunofluorescence to GFAP (green) and AT8 (red). E, F: Double-labeling immunofluorescence to Iba-1 (green) and AT8 (red). G, H: Double-labeling immunofluorescence to Olig2 (green) and AT8 (red).

Subpopulations of neurons (A, B), astrocytes (C, D) and oligodendrocytes (G, H) contain hyper-phosphorylated tau. Hippocampal neurons containing hyper-phosphorylated tau co-express active tau kinase p38. Long arrow: cells with double staining; short arrow: cells only stained green; arrowhead: cells only stained red. Paraffin sections, nuclei stained with DRAQ5™ (blue); bar = 25μm.

Table I: Characteristics of the antibodies used in the present study

Antibody	Mono- /polyclonal	Dilution	Supplier	Country
β -amyloid	monoclonal	1:50	Dako	Glostrup, DK
A β -40	rabbit polyclonal	1:100	Merck-Millipore	Billerica, MA, USA
A β -42	rabbit polyclonal	1:50	Merck-Millipore	Billerica, MA, USA
α -synuclein	rabbit polyclonal	1:500	Chemicon, Merck-Millipore	Billerica, MA, USA
TDP-43	rabbit polyclonal	1:200	Abcam	Cambridge, UK
p62C	guinea pig polyclonal	1:100	Progen, RA Biopharm	Darmstadt, GE
p62N	guinea pig polyclonal	1:100	Progen, RA Biopharm	Darmstadt, GE
Iba1	rabbit polyclonal	1:1000	Wako	Richmond, VA, USA
4Rtau	monoclonal	1:50	Merck-Millipore	Billerica, MA, USA
3Rtau	monoclonal	1:800	Merck-Millipore	Billerica, MA, USA
phospho-tau Thr181	rabbit polyclonal	1:50	Cell Signaling	Danvers, MA, USA
phospho-tau Ser199	rabbit polyclonal	1:50	Calbiochem	Darmstadt, GE
phospho tau Thr231	rabbit polyclonal	1:50	Calbiochem	Darmstadt, GE
phospho-tau Ser262	rabbit polyclonal	1:50	Calbiochem	Darmstadt, GE
phospho-tau Ser422	rabbit polyclonal	1:50	Calbiochem	Darmstadt, GE
AT8 (Ser202/Thr205)	monoclonal	1:50	Innogenetics	Ghent, BE
Tau-100 (Thr212/Ser214)	monoclonal	1:100	Thermo Scientific	Waltham, MA, USA
PHF1(Ser396/Ser404)	monoclonal	1:500	Dr. Peter Davies	New York, USA
Alz50 (aa 5-15)	monoclonal	1:20	Dr. Peter Davies	New York, USA
MC-1 (aa312-322)	monoclonal	1:50	Dr. Peter Davies	USA
tau-C3 (tr Asp421)	monoclonal	1:300	Abcam	Cambridge, UK
Ab 499 (aa 14-26)	monoclonal	1:20	Dr. Jose Luna	CDMX, Mexico DF
Ab 229 (aa 229-233)	rabbit polyclonal	1:100	Dr. Jose Luna	CDMX, Mexico DF
Ab 394 (aa 394-398)	rabbit polyclonal	1:100	Dr. Jose Luna	CDMX, Mexico DF
ubiquitin	rabbit polyclonal	1:200	Dako	Glostrup, DK
glial fibrillary acidic protein (GFAP)	rabbit polyclonal	1:500	Dako	Glostrup, DK
SOD2	rabbit polyclonal	1:100	Stressgen	San Diego, CA, USA
AQP4	monoclonal	1:400	Sigma	St Louis, Missouri, USA
GLT-1	guinea pig	1:100	Merck-Millipore	Billerica, MA, USA
P-GFAP Ser8	Rabbit polyclonal	1:500	Abcam	Cambridge, UK
P-tubulin Ser939	Rabbit polyclonal	1:100	Cell Signaling	Danvers, MA, USA
P-PKA α - β Thr197	Rabbit	1:100	Invitrogen	Carlsbad, CA, USA

P38-P Thr180-Tyr182	polyclonal rabbit polyclonal	1:100	Cell Signaling	Danvers, MA, USA
vimentin	rabbit polyclonal	1:400	Abcam	Cambridge, UK
YKL-40	rabbit polyclonal	1:200	Invitogen	Carlsbad, CA, USA
Olig-2	rabbit polyclonal	1:500	Abcam	Cambridge, UK
NeuN	mouse monoclonal	1:100	Merck-Millipore	Billerica, MA, USA

Table II: Summary of ARTAG cases

THAs: thorn-shaped astrocytes; subepend: subependymal; subpial: subpial; WM T: clusters in the temporal white matter; WM F: clusters in the frontal white matter; perivasc: perivascular; bas foreb: basal forebrain; caudate: caudate nucleus; med obl: medulla oblongata; PART: Primary age-related tauopathy (Braak and Braak staging of NFT pathology); LBD: Lewy body disease; AGD: argyrophilic grain disease.

Case	Age	Gender	Pm delay	THAs									other
				subepend	subpial	WM T	WM F	perivasc	bas foreb	caudate	amygdala	med obl	
1	66	M	8	+	+	+	-	+	+	-	+	-	PART0
2	78	F	4	++	+	++	+	+	+	+	++	++	PARTI
3	87	F	18	++	++	++	+	++	++	+	+	++	PARTI
4	68	M	12	+	++	++	+	+	+	+	+	-	PART I
5	75	M	5h 30 m	++	++	++	++	+	++	+	++	+	PARTII
6	86	M	16	++	++	++	+	+	+	-	+	-	PARTI
7	70	M	17	++	+	++	+	++	+	+	+	-	LBD3
8	86	M	12	++	++	++	+	++	++	+	+	+	AGDI

Table III: List of proteins differentially up-phosphorylated in ARTAG when compared with controls (A) and list of proteins differentially up-phosphorylated in controls when compared with ARTAG (B). See Supplementary Table 1 for details of phosphosites.

(A)

Protein	Accession	Phosphosite/s
1-phosphatidylinositol 4,5-bisphosphate phosphodiesterase delta-3	Q8N3E9	S573
Abl interactor 1	Q8IZP0	S222
Adenylate cyclase type 6	O43306	S54
Amyloid beta A4 protein	P05067	S441
Ankyrin-2	Q01484	S2405
Ankyrin-3	Q12955	S623/T1443/S3055
AP2-associated protein kinase 1	Q2M2I8	S938
Aquaporin-4	P55087	T273
Arf-GAP with SH3 domain, ANK repeat and PH domain-containing protein 1	Q9ULH1	S1008
ATP-dependent 6-phosphofructokinase, platelet type	Q01813	T313
B-cell lymphoma/leukemia 11A	Q9H165	S608
Beta-2-syntrophin	Q13425	S95
Brefeldin A-inhibited guanine nucleotide-exchange protein 1	Q9Y6D6	S1079
Brefeldin A-inhibited guanine nucleotide-exchange protein 2	Q9Y6D5	S277
C-Jun-amino-terminal kinase-interacting protein 3	Q9UPT6	T275
C-type mannose receptor 2	Q9UBG0	S1457
Calcium-binding and coiled-coil domain-containing protein 1	Q9P1Z2	S563
Calcium/calmodulin-dependent 3',5'-cyclic nucleotide phosphodiesterase 1C	Q14123	S469
Calcium/calmodulin-dependent protein kinase type II subunit gamma	Q13555	S276
Calmodulin-regulated spectrin-associated protein 3	Q9P1Y5	S553
cAMP-dependent protein kinase catalytic subunit alpha	P17612	T198/S339
cAMP-regulated phosphoprotein 19	P56211	S104
cAMP-specific 3',5'-cyclic phosphodiesterase 4B	Q07343	S290
CAP-Gly domain-containing linker protein 3	Q96DZ5	S402
Capping protein, Arp2/3 and myosin-I linker protein 2	Q6F5E8	S991
Catenin beta-1	P35222	S552/S675
Catenin delta-2	Q9UQB3	S201/S285

Centriole, cilia and spindle-associated protein	Q6IQ19	S240
Clathrin coat assembly protein AP180	O60641	S296
Clathrin interactor 1	Q14677	S227/S299
Creatine kinase B-type	P12277	T322
Creatine kinase U-type, mitochondrial	P12532	S318
Cyclin-dependent kinase 12	Q9NYV4	S1082
Cysteine-rich protein 2	P52943	S114
Dematin	Q08495	S11
Dendrin	O94850	S567
DENN domain-containing protein 4B	O75064	S736
Dihydropyrimidinase-related protein 1	Q14194	T509
Disks large-associated protein 1	O14490	S397
DNA repair protein XRCC1	P18887	S241
E3 ubiquitin-protein ligase UBR4	Q5T4S7	T2724
FERM, RhoGEF and pleckstrin domain-containing protein 1	Q9Y4F1	S427
Glial fibrillary acidic protein	P14136	S8/Y14/S82/S424
Glutamate receptor-interacting protein 1	Q9Y3R0	S953
Glycylpeptide N-tetradecanoyltransferase 2	O60551	S68
Growth arrest-specific protein 7	O60861	S163
Guanine nucleotide-binding protein G(I)/G(S)/G(O) subunit gamma-12	Q9UBI6	S7
IQ motif and SEC7 domain-containing protein 1	Q6DN90	S105
Junctional protein associated with coronary artery disease	Q9P266	S757
Kinase suppressor of Ras 2	Q6VAB6	S474
LIM and calponin homology domains-containing protein 1	Q9UPQ0	S670
Liprin-alpha-2	O75334	S774
LysM and putative peptidoglycan-binding domain-containing protein 2	Q8IV50	S24
MAP7 domain-containing protein 1	Q3KQU3	S544
Microtubule-associated protein 1A	P78559	S384/T2655
Microtubule-associated protein 1B	P46821	S2271
Microtubule-associated protein 1S	Q66K74	S759
Microtubule-associated protein 2	P11137	T1631
Microtubule-associated protein tau	P10636	T529/S579
Monoglyceride lipase	Q99685	S301
N-alpha-acetyltransferase 10	P41227	S205

Neurofilament medium polypeptide	P07197	S558
NSFL1 cofactor p47	Q9UNZ2	S114
Nuclear receptor coactivator 5	Q9HCD5	S6
Nucleolar and coiled-body phosphoprotein 1	Q14978	S264
Oxidation resistance protein 1	Q8N573	S7
Paralemmin-1	O75781	T145/S162
Phosphoglycerate kinase 1	P00558	Y76
Plakophilin-4	Q99569	S776
Plectin	Q15149	S2039
Potassium voltage-gated channel subfamily A member 2	P16389	S441
Protein bassoon	Q9UPA5	S1362
Protein cordon-bleu	O75128	S235
Protein ELFN1	P0C7U0	S461
Protein kinase C alpha type	P17252	S226
Protein kinase C epsilon type	Q02156	S346
Protein phosphatase 1 regulatory subunit 1A	Q13522	S6
Rabankyrin-5	Q9P2R3	S861
Ral GTPase-activating protein subunit alpha-1	Q6GYQ0	S740
Ras-specific guanine nucleotide-releasing factor 2	O14827	S848
Reticulon-1	Q16799	T300
Serine/arginine-rich splicing factor 5	Q13243	S233
Serine/arginine repetitive matrix protein 1	Q8IYB3	S675
Signal-induced proliferation-associated 1-like protein 2	Q9P2F8	S194
SLIT-ROBO Rho GTPase-activating protein 3	O43295	S1068
Sorbin and SH3 domain-containing protein 1	Q9BX66	T497
Spectrin alpha chain, non-erythrocytic 1	Q13813	S1031
Spectrin beta chain, non-erythrocytic 4	Q9H254	S2254
Synapsin-1	P17600	S568
Synaptophysin	P08247	Y81
Synaptopodin	Q8N3V7	S754
Syntaphilin	O15079	S200/S204
T-complex protein 1 subunit delta	P50991	T239
Tau-tubulin kinase 1	Q5TCY1	S456
TBC1 domain family member 10B	Q4KMP7	S678
Thy-1 membrane glycoprotein	P04216	S24

Tight junction protein ZO-1	Q07157	S1278
Tight junction protein ZO-2	Q9UDY2	S266
Tripartite motif-containing protein 2	Q9C040	S10
Tuberin	P49815	S939
Ubiquitin-associated protein 2-like	Q14157	S467
Ubiquitin carboxyl-terminal hydrolase CYLD	Q9NQC7	S399
UHRF1-binding protein 1-like	A0JNW5	S989
Uncharacterized protein C9orf172	C9J069	S484
Uncharacterized protein KIAA1211-like	Q6NV74	S653
Voltage-dependent P/Q-type calcium channel subunit alpha-1A	O00555	S2463
WAS/WASL-interacting protein family member 3	A6NGB9	T208
Zinc finger CCCH domain-containing protein 18	Q86VM9	S534
Zinc finger Ran-binding domain-containing protein 2	O95218	S153

(B)

Protein	Accession	Phosphosite/s
2',3'-cyclic-nucleotide 3'-phosphodiesterase	P09543	S64/S327
60 kDa heat shock protein, mitochondrial	P10809	S70
Ankyrin repeat domain-containing protein 27	Q96NW4	S634
AP-3 complex subunit beta-2	Q13367	S272
Arf-GAP with GTPase, ANK repeat and PH domain-containing protein 1	Q9UPQ3	S421
Band 4.1-like protein 2	O43491	S550
Caskin-1	Q8WXD9	S1257
Catenin alpha-2	P26232	S654
E3 ubiquitin-protein ligase HUWE1	Q7Z6Z7	S2362
Guanine nucleotide-binding protein G(I)/G(S)/G(O) subunit gamma-2	P59768	T52
Hepatocyte cell adhesion molecule	Q14CZ8	S377
Heterogeneous nuclear ribonucleoprotein U-like protein 2	Q1KMD3	T165
Huntingtin-interacting protein 1	O00291	S320
Inactive ubiquitin carboxyl-terminal hydrolase 54	Q70EL1	S481
Microtubule-associated protein 1B	P46821	S970/S995/S1322
Microtubule-associated protein 4	P27816	S507/T521
Microtubule-associated protein 6	Q96JE9	S812
Nuclear receptor-binding protein	Q9UHY1	S2
Nucleolar protein 56	O00567	S569
Pecanex-like protein 3	Q9H6A9	S1955
Potassium voltage-gated channel subfamily KQT member 2	O43526	S472
Protein kinase C gamma type	P05129	T655

Rho GDP-dissociation inhibitor 1	P52565	S24
Rho guanine nucleotide exchange factor 7	Q14155	S249
Serrate RNA effector molecule homolog	Q9BXP5	S4
Transcription intermediary factor 1-beta	Q13263	S594
Transmembrane protein 229A	B2RXF0	S4
Tumor protein D52	P55327	S144
UV excision repair protein RAD23 homolog A	P54725	S123
Vinculin	P18206	S290/S346
Vinexin	O60504	S545

Table IV: Phosphorylation sites of selected proteins in ARTAG

Isoform Name	Peptide Sequence	Position Peptide	Position Protein
Glial fibrillary acidic protein	RSYVSSGEMMVGGLAPGR	3	14
Glial fibrillary acidic protein	DGEVIKESK	8	424
Glial fibrillary acidic protein	RITSAAR	4	8
Glial fibrillary acidic protein	FASYIEK	3	82
Isoform Tau-C of Microtubule-associated protein tau	TPSLPTPPTR	1	212
Isoform Tau-C of Microtubule-associated protein tau	IGSTENLK	3	262
Potassium voltage-gated channel subfamily A member 2	IPSSPDLK	4	441
cAMP-dependent protein kinase catalytic subunit alpha	TWTLCGTPEYLAPEILSK	3	198
cAMP-dependent protein kinase catalytic subunit alpha	GPGDTSNFDDYEEEEIRVSINEK	19	339
Catenin beta-1	RTSMGGTQQQFVEGVR	3	552
Catenin beta-1	RLSVELTSSLFR	3	675
Microtubule-associated protein 1A	STTSQVTPEEK	7	2655
Microtubule-associated protein 1B	SKPLAASPAPGLK	7	2271
Tuberin	STSLNERPK	3	939
Aquaporin-4	AAQQTKGSYMEVEDNR	5	273
Protein phosphatase 1 regulatory subunit 1A	MEQDNSPRK	6	6
Calcium/calmodulin-dependent protein kinase type II subunit gamma	STVASMMHR	1	276
Calcium/calmodulin-dependent 3',5'-cyclic nucleotide phosphodiesterase 1C	RSSLNSISSDAK	3	469
Tau-tubulin kinase 1	VNSPESER	3	456
C-Jun-amino-terminal kinase-interacting protein 3	SNTPSSVPSAAVTPLNESLQPLGDYGVGSK	3	275
Catenin delta-2	ATGQSFSQGTTSR	5	201
Catenin delta-2	GGSAPEGATYAAPR	3	285
Neurofilament medium polypeptide	EGSSKEEEGEQEEGETEAEAEAEAEAEKEEK	3	558